

8-1-2023

Sea Ice Formation, Glacial Melt and the Solubility Pump Boundary Conditions in the Ross Sea

Brice Loose
University of Rhode Island

Sharon Stammerjohn
University of Colorado Boulder

Peter Sedwick
Old Dominion University

Stephen Ackley
The University of Texas at San Antonio

Follow this and additional works at: <https://digitalcommons.uri.edu/gsofacpubs>

Citation/Publisher Attribution

Loose, Brice, Sharon Stammerjohn, Peter Sedwick, and Stephen Ackley. "Sea Ice Formation, Glacial Melt and the Solubility Pump Boundary Conditions in the Ross Sea." *Journal of Geophysical Research: Oceans* 128, 8 (2023). doi: [10.1029/2022JC019322](https://doi.org/10.1029/2022JC019322).

This Article is brought to you by the University of Rhode Island. It has been accepted for inclusion in Graduate School of Oceanography Faculty Publications by an authorized administrator of DigitalCommons@URI. For more information, please contact digitalcommons-group@uri.edu. For permission to reuse copyrighted content, contact the author directly.

Sea Ice Formation, Glacial Melt and the Solubility Pump Boundary Conditions in the Ross Sea

Keywords

air/sea exchange; dense shelf water; noble gases; polynya; solubility pump

Creative Commons License



This work is licensed under a [Creative Commons Attribution-Noncommercial 4.0 License](https://creativecommons.org/licenses/by-nc/4.0/)

Sea Ice Formation, Glacial Melt and the Solubility Pump Boundary Conditions in the Ross Sea

 Brice Loose¹ , Sharon Stammerjohn² , Peter Sedwick³ , and Stephen Ackley⁴ 

¹Graduate School of Oceanography, University of Rhode Island, Narragansett, RI, USA, ²Institute of Arctic and Alpine Research, University of Colorado, Boulder, CO, USA, ³Department of Ocean and Earth Sciences, Old Dominion University, Norfolk, VA, USA, ⁴Center for Advanced Measurements in Extreme Environments, University of Texas at San Antonio, San Antonio, TX, USA

Key Points:

- Noble gas tracers can infer the rate of sea ice production in polynyas
- Frazil ice in polynyas appears to block air-sea gas exchange mechanisms
- The solubility pump is influenced by glacial ice melt and sea ice formation

Supporting Information:

Supporting Information may be found in the online version of this article.

Correspondence to:

B. Loose,
bloose@uri.edu

Citation:

Loose, B., Stammerjohn, S., Sedwick, P., & Ackley, S. (2023). Sea ice formation, glacial melt and the solubility pump boundary conditions in the Ross Sea. *Journal of Geophysical Research: Oceans*, 128, e2022JC019322. <https://doi.org/10.1029/2022JC019322>

Received 1 OCT 2022

Accepted 27 JUL 2023

Author Contributions:

Conceptualization: Brice Loose, Sharon Stammerjohn

Formal analysis: Brice Loose

Funding acquisition: Brice Loose

Methodology: Brice Loose, Sharon Stammerjohn, Stephen Ackley

Project Administration: Brice Loose

Supervision: Brice Loose

Validation: Peter Sedwick

Writing – original draft: Brice Loose, Sharon Stammerjohn, Peter Sedwick, Stephen Ackley

Writing – review & editing: Sharon Stammerjohn, Peter Sedwick, Stephen Ackley

Abstract Seasonal formation of Dense Shelf Water (DSW) in the Ross Sea is a direct precursor to Antarctic Bottom Water, which fills the deep ocean with atmospheric gases in what composes the southern limb of the solubility pump. Measurements of seawater noble gas concentrations during katabatic wind events in two Ross Sea polynyas reveal the physical processes that determine the boundary value properties for DSW. This decomposition reveals 5–6 g kg⁻¹ of glacial meltwater in DSW and sea-ice production rates of up to 14 m yr⁻¹ within the Terra Nova Bay polynya. Despite winds upwards of 35 m s⁻¹ during the observations, air bubble injection had a minimal contribution to gas exchange, accounting for less than 0.01 μmol kg⁻¹ of argon in seawater. This suggests the slurry of frazil ice and seawater at the polynya surface inhibits air-sea exchange. Most noteworthy is the revelation that sea-ice formation and glacial melt contribute significantly to the ventilation of DSW, restoring 10% of the gas deficit for krypton, 24% for argon, and 131% for neon, while diffusive gas exchange contributes the remainder. These measurements reveal a cryogenic component to the solubility pump and demonstrate that while sea ice blocks air-sea exchange, sea ice formation and glacial melt partially offset this effect via addition of gases. While polynyas are a small surface area, they represent an important ventilation site within the southern-overturning cell, suggesting that ice processes both enhance and hinder the solubility pump.

Plain Language Summary Previous scientific studies have demonstrated that the water which fills the deep sea is created in isolated regions of the surface ocean where wind, evaporation, heat loss, and sea ice formation can work in concert to make very cold salty seawater at the ocean surface. As this water leaves the surface it can carry oxygen and carbon dioxide, as well as heat away from the atmosphere for nearly a millennium, suggesting the sequestration mechanism may impact earth's climate and human climate change. This study sought to reveal how different types of sea ice and glacier ice might influence the gases that are dissolved in seawater and sequestered in the ocean. We made measurements of the noble gases (helium, neon, argon, krypton, and xenon) in the Ross Sea in late fall of 2017, when the conditions are cold and windy, leading to lots of dense water production. The results reveal that sea ice interrupts the process of air-sea exchange of gases, which can slow down the uptake of human-generated carbon dioxide by dense water. But our results also revealed that sea ice formation and glacial ice melt can both add gas to dense water during its creation.

1. Introduction

Latent heat polynyas are veritable ice factories, producing a quantity of ice cover that is far out of proportion to their surface area: As much as 10% of the Antarctic ice pack is produced within an area that is ca. 1% of the seasonal maximum in ice extent (Tamura et al., 2008). This disproportionate sea ice production rate makes these features an essential component to the ventilation of Antarctic Bottom Water (AABW) (Gordon et al., 2010; Silvano et al., 2020), which is a mixture of Circumpolar Deep Water (CDW), the warmest water mass in the Southern Ocean, and the Dense Shelf Water (DSW), the cold, salty precursor to AABW, and originates within these polynyas. In the satellite era, there has been only one documented occurrence of a sensible heat polynya, which are driven by upwelling of ocean sensible heat (Cheon et al., 2015; de Lavergne et al., 2014), suggesting Antarctic latent heat polynyas, which are maintained by katabatic winds, are the primary mechanism of DSW production and thus ventilation of the deep Southern limb of the meridional overturning circulation (MOC).

© 2023 The Authors.

This is an open access article under the terms of the [Creative Commons Attribution-NonCommercial License](https://creativecommons.org/licenses/by-nc/4.0/), which permits use, distribution and reproduction in any medium, provided the original work is properly cited and is not used for commercial purposes.

The importance of polynyas to the MOC also signifies that they play a disproportionate role in controlling the dissolution of carbon dioxide and oxygen, for example, in AABW (Ohshima et al., 2016). Continental shelf processes that lead to upwelling, entrainment, and biogeochemical modifications therefore help to set the properties for AABW and control the solubility pump (Jacobs & Giulivi, 2010). The role of sea-ice cover and the size of the outcropping region in models of the MOC are considered to be a key component of the solubility pump efficiency: as the area of the outcrop region shrinks (Nicholson et al., 2010; Toggweiler et al., 2003) or becomes ice-covered (Sigman et al., 2010; Stephens & Keeling, 2000), it enhances the ocean-atmosphere $p\text{CO}_2$ differential and weakens the solubility pump (Broecker et al., 1999; Toggweiler et al., 2003). This phenomenon may also impact the ocean-atmosphere oxygen differential, which suggests a reinterpretation of the oxygen decreases during glacial periods, because the oxygen content in newly formed deep water is overestimated (Cliff et al., 2021).

That insight from models suggests that deep water formation in polynyas, which are disproportionately small by surface area, is perhaps the least efficient mechanism to support a robust solubility pump. However, these studies have focused exclusively on the role of sea-ice cover in reducing or inhibiting air-sea exchange (e.g., Stephens & Keeling, 2000). In this study we document the role of physical processes that take place within the polynya and over the continental shelf, and we assess how these processes contribute to setting the gas solubility properties of DSW. We argue that ice processes—sea ice formation and glacier melt—act to restore a significant portion of the solubility deficit that arises as CDW upwells and is modified into DSW. We use measurements of the five inert noble gases to constrain the impact of these physical processes and we develop a budget closure for three noble gases with unique sources and solubilities to reveal how each process contributes to the ultimate gas solubility properties observed in DSW.

1.1. Ross Sea Waters, the Regional Context and Noble Gas Distributions

Circumpolar Deep Water upwells latitudinally near 60°S within the Antarctic Divergence Zone (Jenkins, 2020), and the Ross Sea receives cross-shore inputs of modified CDW, which originates from the east within the Ross Gyre, and flows along the continental shelf break. This shelf-adjacent water mass is described as a 1,000 m thick layer with temperature greater than 0.6°C (Orsi & Wiederwohl, 2009). The CDW in this region contributes significantly to the shelf break frontal system that moves intermittently onshore and offshore, releasing DSW in tidal pulses (Padman et al., 2009). These tidal currents can reach speeds of 1 m s^{-1} , particularly within the concentrated outflow regions found at the Drygalski, Joides, and Glomar Challenger Troughs in the Western Ross Sea. It further appears that these dense outflows are connected to the onshore flow of CDW. Morrison et al. (2020) used an eddy-resolving model to reveal inflows of CDW that coincide spatially and temporally with the pulsed outflow of DSW.

The Ross Sea has been experiencing a secular decrease in salinity (Jacobs et al., 2002), a process that has been associated with freshening of DSW (Silvano et al., 2020), perhaps as a consequence of increased glacial melting in the Amundsen and eastern Ross Seas, which lie upstream along the Antarctic Coastal Current (Jacobs & Giulivi, 2010). In Prydz Bay, East Antarctica, inputs of submarine Glacial Meltwater (GMW) into DSW have been shown to moderate dense water production (Williams et al., 2016). A recent study has documented a rebound in the salinity of DSW (Silvano et al., 2018), revealing how winds and the rate of regional sea ice production are direct drivers of DSW production on a seasonal basis, but the trend of Ross Sea freshening appears to persist over decades to the present day (Jacobs et al., 2022). Collectively, these studies reinforce that there is a complex and fundamental connection between the Antarctic ice processes and the MOC.

The five stable noble gases—helium, neon, argon, krypton, xenon, reveal the range of processes operating on dissolved gases in the actively ventilated layers of the Ross Sea continental shelf. Helium and neon, the lightest noble gases, exhibit low solubility in seawater, but elevated concentrations in glacial ice, which traps on average 110 ml of air per kg of ice (Martinerie et al., 1992).

Krypton and xenon are heavier and increasingly more soluble noble gases; their temperature-dependent solubility and slower gas exchange rates produce water column deficits during the cooling period with restricted air-sea exchange (Hamme et al., 2019), revealing that noble gas isotope and elemental ratios may be able to constrain net air-sea exchange (Seltzer et al., 2019). The addition of melted glacial ice can also lead to a slight deficit in Kr and Xe (Loose & Jenkins, 2014), which further helps to distinguish glacial melt from air bubble injection. In

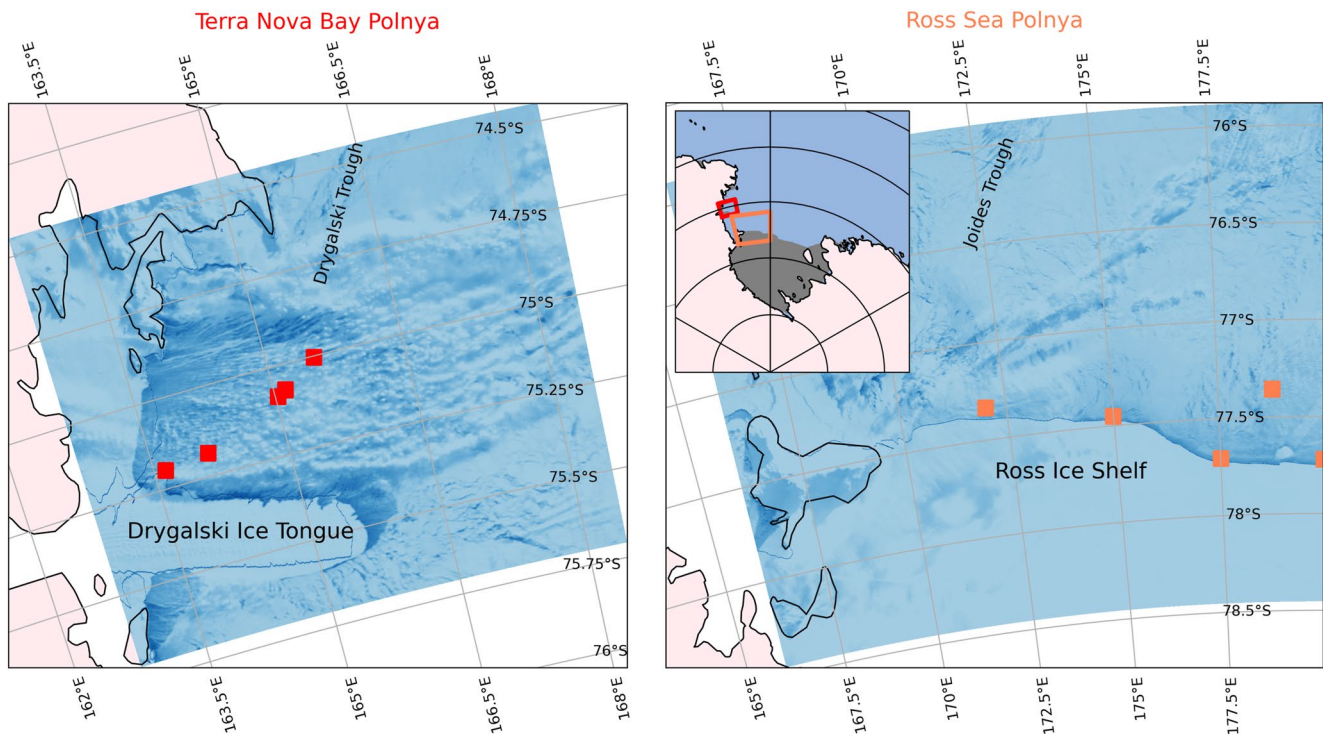


Figure 1. Map of the Terra Nova Bay (a) and Ross Sea (b) Polynyas. Square symbols indicate the hydrographic station locations. The inset in panel B reveals the location of both polynyas within the Ross Sea. Moderate Resolution Imaging Spectroradiometer visible imagery shows surface conditions at the end of March 2017 when light was still sufficient for visible imaging. The light blue colors are either ice or the limited cloud cover, and the dark blue colors represent thin ice or open water.

addition to air-sea disequilibrium and GMW, sea ice formation may alter the water column dissolved gas budgets under certain conditions (Top et al., 1988). This is caused by solute exclusion and brine rejection from the sea ice crystal lattice during freezing (Hood et al., 1998; Namiot & Bukhgalter, 1965). In coastal polynyas the exceedingly high rates of sea ice formation (Ohshima et al., 2013; Tamura et al., 2008) may be sufficient to influence the water column noble gas excesses (Loose et al., 2016). Solute exclusion is more intensive for the heavier dissolved solutes (Killawee et al., 1998). This process can lead to greater exclusion of for example, Kr and Xe during freezing as compared to Ne and He.

The noble gases can be used to reconstruct the impacts of solute inputs from sea ice production, freshening from GMW, and diffusive air-sea disequilibrium at the time of DSW formation. We use the noble gas paleothermometer (NGPT) inverse model (Aeschbach-Hertig & Solomon, 2013; Stute & Schlosser, 1993) to infer each of the contributions to shelf water (SW) in the Ross Ice Shelf polynya (RSP) and the Terra Nova Bay polynya (TNBP).

2. Methods

2.1. PIPERS Field Campaign

The measurements used in this study were collected during austral fall, between 1 May and 26 May 2017 during the Polynyas and Ice Production in the Ross Sea (PIPERS) expedition (Ackley et al., 2020). Individual conductivity temperature depth sensor (CTD) profiles and water-column samples were collected in the TNBP and the RSP (Figure 1). Conditions in the TNBP were significantly windier than in the RSP, with a mean wind speed of 20.3 m s^{-1} between April and October, as compared to 5.7 m s^{-1} as measured by Automated Weather Stations Manuela (near TNBP) and Vito (near RSP). These mean wind differences reveal themselves in the water column properties (as discussed below).

Noble gas samples were collected from a 24-bottle 20L Niskin rosette using the copper tube cold-weld method (Loose et al., 2016). Extracted gas samples are measured using an automated dual mass spectrometric system and

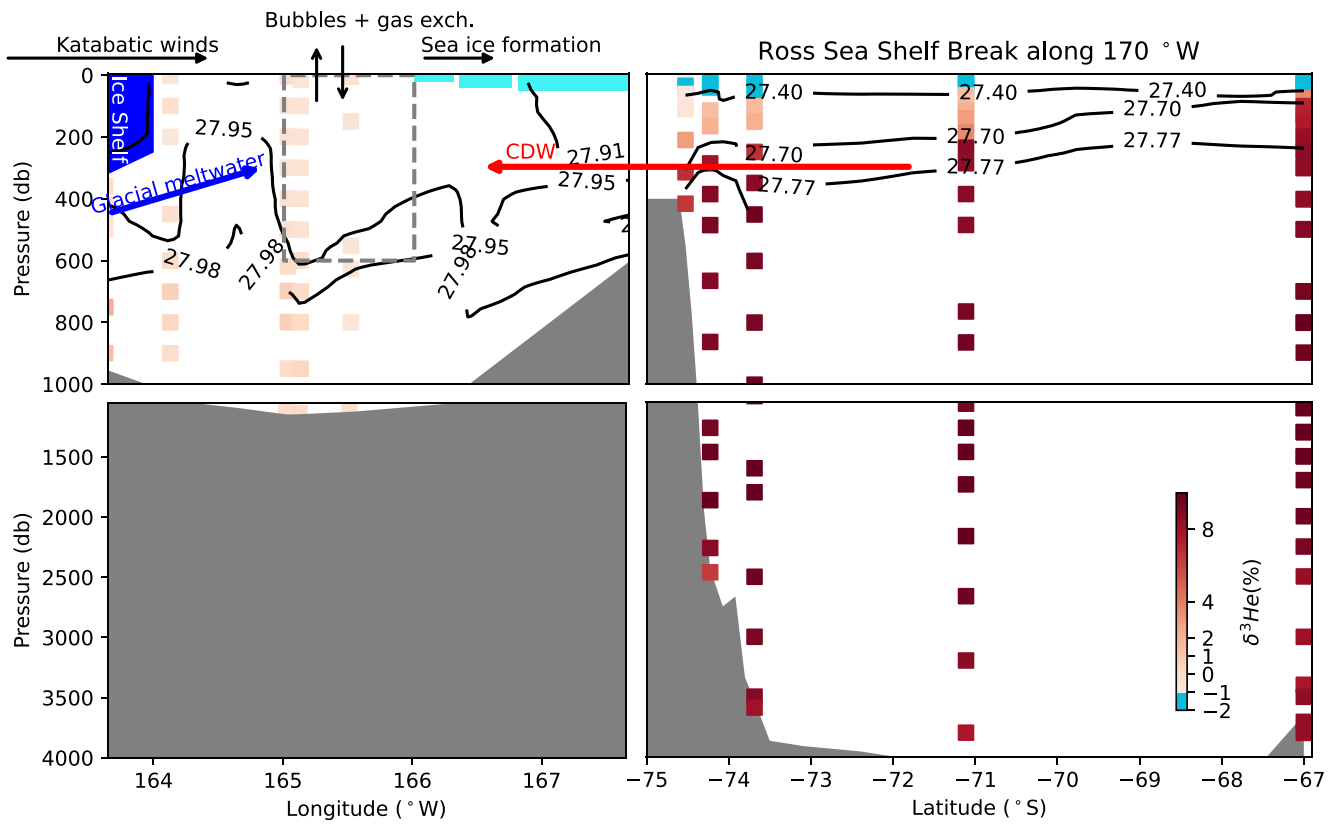


Figure 2. Profiles of $\delta^3\text{He}$ beyond the continental shelf along 170°W , collected during the Climate Variability and Predictability Program 2011 s04p line, and within Terra Nova Bay polynya, during the 2017 Polynyas and Ice Production in the Ross Sea expedition. The $\delta^3\text{He}$ traces the on-shore transport of circumpolar deep water and the ventilation process that takes place within the polynya. The black contours are lines of seawater potential density anomaly. The gray filled area represents the bottom topography. The schematic arrows depict the contributions of individual processes and water masses to the water column profiles in the polynya box, indicated by a dashed line.

analyzed for $\delta^3\text{He}$, He, Ne, Ar, Kr, and Xe (Stanley, Baschek, et al., 2009). Precision was determined by extracting and analyzing $N = 9$ duplicate copper tubes as 0.25%, 0.22%, 0.14%, 0.14%, 0.26%, and 0.35% for $\delta^3\text{He}$, He, Ne, Ar, Kr, and Xe respectively.

2.2. The Noble Gas Paleothermometer

The NGPT attempts to distinguish the physical processes that establish dissolved gas and thermohaline properties of surface water as it is modified to become interior water. The method was originally developed to quantify air entrainment during groundwater aquifer recharge (Aeschbach-Hertig & Solomon, 2013; Stute & Schlosser, 1993). In this study and in Loose et al. (2016) we have adapted the NGPT to observe the transformation of CDW into DSW through diffusive air-sea gas exchange (driven mostly by rapid cooling of the water parcel), air bubble injection, GMW inclusion, and sea ice formation. Unlike the original NGPT, this model does not reconstruct water temperature, so it represents a modified-NGPT or mNGPT. The descriptive picture of CDW crossing the shelf break to be being acted upon by strong winds and cold air temperatures which lead to extreme heat loss and in-situ formation of frazil ice, can be seen from the $\delta^3\text{He}$ tracer fields in Figure 2. Helium-3 labels CDW and illustrates the remnant properties of CDW that can be found on the continental shelf, in spite of the intense water mass ventilation processes. During the PIPERS expedition, frazil ice formation was extensive throughout the TNBP during two katabatic wind events (Ackley et al., 2020; Tison et al., 2020). During the specific conditions when we observed frazil ice formation, temperature and salinity anomalies in the surface ocean were observable during repeated CTD profiles (Thompson et al., 2020).

Referring to the schematic polynya box (dashed line in Figure 2), the mNGPT begins with a mass conservation statement, which also reveals how polynya processes lead to modifications of the individual water properties. The

Table 1
List of Properties for Each of the End Member Values and Free Parameters in the Noble Gas Paleothermometer Model

	Heat (°C)	Salt (gkg ⁻¹)	He (μmol kg ⁻¹)	Ne (μmol kg ⁻¹)	Ar (μmol kg ⁻¹)	Kr (μmol kg ⁻¹)	Xe (μmol kg ⁻¹)
SW	T_{obs}	Free param. of interest	Free param. of interest: $[\beta_i(S_{\text{sw}}, T)\chi_i + A\chi_i]f_{\text{sw}}$				
CDW	1.63	34.7	0.0019	0.008	16.25	0.0039	0.0006
GMW	-92	0	0.025	0.086	44.23	0.005	0.004
ICE	$T_{\text{obs}} + 0.167f_{\text{sw}} \frac{L_f}{C_{p,\text{sw}}}$	$0.33S_{\text{sw}}$	Free param. of interest: $\beta_i(S_{\text{sw}}, T)\chi_i\kappa_{\text{iw}}$				
S_{sw}	N/I	Free param. of interest	N/I	N/I	N/I	N/I	N/I
Air	N/I	N/I	Free param. of interest: $A\chi_i$				

Note. The values for CDW were determined using off-shelf profiles from the Weddell and Amundsen Seas (Biddle et al., 2019; Loose et al., 2016). The values for GMW were derived using the average air content of glacial ice from Martinerie et al. (1992), and the values for f_{ice} were determined using the equilibrium partition coefficient defined in Equation 3, for He: 1.33, Ne: 0.83, Ar: 0.49, Kr: 0.4, Xe: 0.5. The N/I terms signify values that were “not included” because the individual tracer (column) has no impact on the given process or water mass (row).

observed inert noble gas concentrations are used to constrain a gas molar mass balance within SW, CDW, GMW, and the gas lost to sea ice (Ice):

$$M_{\text{obs}} = M_{\text{sw}} - M_{\text{ice}} + M_{\text{gmw}} + M_{\text{cdw}} \quad (1)$$

M_{ice} refers to the moles of gas that have been removed during sea ice formation and advection by surface winds, and is explicitly defined as a loss term. We can simplify the conservation statement by first expressing the masses of each tracer as the product of the volume of seawater or sea ice (e.g., V_{gmw} is the volume of GMW), ρ is the density of water or ice, P_{slp} is the sea level pressure, and C is the concentration in micromoles per kilogram of seawater. Note, we have made the approximation that the differences in density between the water masses are small enough to be neglected:

$$C_{\text{obs}}V_{\text{tot}}\rho_w = [\beta(S, T, P_{\text{slp}})\chi + A\chi]V_{\text{sw}}\rho_w - \rho_{\text{ice}}C_{\text{ice}}V_{\text{ice}} + V_{\text{gmw}}C_{\text{gmw}}\rho_w + V_{\text{cdw}}C_{\text{cdw}}\rho_w \quad (2)$$

In Equation 2 we have explicitly defined tracer concentration in SW as:

$$C_{\text{sw}} = [\beta(S, T, P_{\text{slp}})\chi + A\chi] \quad (3)$$

The two terms on the right of Equation 3 represent the atmospheric gases in SW. These are determined using the equilibrium solubility coefficient (β , Jenkins et al., 2019) and the molar mixing ratio of each gas in air, (χ), which is constant for each of the noble gases. The mass of each gas injected through air bubbles is the product of the molar concentration of air dissolved in water (A) with χ , the molar mixing ratio. A cannot be less than zero.

Sea ice formation results in the partitioning of dissolved solutes between brine pockets that are included within the ice, and dissolved solutes that are immediately or eventually deposited in the water parcel beneath sea ice (Killawee et al., 1998). This process of solute exclusion is complex and evolves through several phases that include near instantaneous segregation during formation of individual ice crystals as well as the nucleation of bubbles at the freezing interface (Crabeck et al., 2015), and brine drainage, which happens over time as the individual brine pockets coalesce into brine channels (Feltham et al., 2006; Wettlaufer, 1992). Here, the treatment of brine drainage and solute exclusion is somewhat coarse, but is an adequate approximation given what residual solutes can be measured in the water column. The near-equilibrium partitioning between the concentration of solutes in ice (C_{ice}) can be related to the concentration of the same solute found in the ambient water (C_{eq}) in our case.

$$\kappa_{\text{iw}} = \frac{C_{\text{ice}}}{C_{\text{eq}}} \quad (4)$$

The term κ_{iw} is the ice-water partition coefficient (Garandet et al., 1994) and it has been estimated for a variety of solutes, including the noble gases and salt. Here, dissolved helium is unique from the larger noble gases, because it appears to prefer incorporation into the sea ice lattice structure, producing a value of $\kappa_{\text{iw}} > 1$. All other gases are preferentially excluded. The values of κ_{iw} are individually listed in the caption of Table 1.

Because it is not practical to make direct measurements of C_{ice} the tracer concentration in the ice, Equation 3 can be used to substitute C_{ice} for C_{eq} in Equation 2. This permits the expression of the mass of sea ice water removed in terms of the ambient tracer concentrations (C_{eq}): $C_{ice} = \kappa_{iw} C_{eq}$. By dividing the R.H.S. of Equation 2 by V_{tot} , we obtain the water mass fractions that characterize the mNGPT, for example, $f_{gmw} = \frac{V_{gmw}}{V_{tot}}$. Gathering the terms, Equation 2 simplifies to:

$$C_{obs} = [\beta(S_{sw}, T, P_{slp})\chi + A\chi](f_{sw}) - \kappa_{iw}\beta(S_{sw}, T)_{sw}\chi \frac{\rho_{ice}}{\rho_{sw}} f_{ice} + f_{gmw}C_{gmw} + f_{cdw}C_{cdw} \quad (5)$$

Equation 4 expresses the observed concentration in terms of the unknown properties of interest: f_{sw} , f_{ice} , f_{gmw} , f_{cdw} , A , and S_{sw} . Respectively, these are the water mass fractions, the moles of air per kg of seawater, and the salinity of SW. The term S_{sw} is allowed to vary as a parameter in the model to reflect the likelihood that the gas in SW is not in equilibrium with the atmosphere and will therefore lead to diffusive gas exchange (Loose et al., 2016). As with Loose et al. (2016), we use a constant pressure value. The long-term average of sea level pressure is 0.9719 ± 0.0036 atm reflecting the persistent low pressure over the latitudes of the Ross Sea (Allan & Ansell, 2006; Costanza et al., 2016). Given the results from automated weather station data, this is a reasonable approximation and reduces the ambiguities in the NGPT model that can result from the non-linear terms. During the PIPERS expedition, most of the water column in the TNBP and RSP was at or below the freezing point, so the temperature parameter space is restricted at the lower limit leading us to use the observed temperature and remove temperature as a free parameter from the model. Equation 5 requires a non-linear optimization technique to account for the changes in β , which are non-linearly dependent on S_{sw} . Further details on the optimization can be found in Loose et al. (2016).

In addition to Equation 5, water continuity provides an additional constraint to ensure that all the water mass fractions sum to 1 (Equation S1 in Supporting Information S1). Equation 5 is nearly identical for salt conservation. As with the other dissolved solutes, salt is excluded during the seawater freezing process: bulk sea ice salinity is typically $\frac{1}{3}$ of the salinity found in the subnatant seawater (Thomas & Dieckmann, 2010). Therefore, we employ a partition coefficient of $\kappa_{iw} = 0.33$ for salt. Salinity is not a volatile solute, so it is neither affected by air-sea gas exchange nor air bubble injection (Equation S2 in Supporting Information S1).

The argument for the heat budget is slightly different from the salt budget. Heat transfer at the air-sea interface has many pathways, including latent, sensible, and radiative heat transfer. There is no known partitioning coefficient for heat exclusion from sea ice. However, freezing is accompanied by a heat loss in the form of latent heat. Away from the air-sea interface, we argue that all this heat transfer takes place between the liquid and solid phase of H_2O (Gade, 1979; Jenkins, 1999). This is the argument used to define the GMW end member. Sea ice formation is not as straightforward, because much of the latent heat is likely lost to the atmosphere. During PIPERS, Thompson et al. (2020) observed anomalies, or bulges in the otherwise vertical profiles of heat and salt directly beneath the air-water interface in the intense periods of katabatic wind activity. These anomalies were concluded to be the result of ice formation. In their budget analyses, the mass of heat and salt were not proportionate. Instead, the excess heat was about 25% of the excess salt. As stated above, long-term observations indicate that sea ice achieves an average salinity that is approximately 33% of the seawater salinity before freezing. These suggest a “partition coefficient” for heat that is $0.25 \times (1 - 0.33) = 16.7\%$ of the initial heat content.

To formulate the heat budget during sea ice formation, we first imagine that no heat is lost to the atmosphere, so the heat balance is:

$$Q_w = Q_{ice} + Q_{lf} \quad (6)$$

where Q_w is the heat content of water being converted to sea ice, and Q_{lf} is the heat transferred by latent heat release. Expanding the heat balance equation using ρ , c_p , T , V the density, specific heat capacity, temperature and volume gives:

$$\rho_w V_w c_{p,sw} T_w = \rho_{ice} V_{ice} c_{p,ice} T_{ice} + \rho_{ice} V_{ice} L_f \quad (7)$$

The term L_f is the latent heat of fusion in Joules per kg of water. The heat budget for sea ice formation is next substituted into the heat conservation equation, which mirrors Equation 5:

$$Q_{obs} = Q_{sw} - Q_{ice} + Q_{cdw} + Q_{gmw} \quad (8)$$

Table 2
Estimates of the Average and 95% Confidence Intervals From Monte Carlo Resampling of the mNGPT Model Solution

	f_{sw} (%)	f_{cdw} (%)	f_{gmw} (%)	f_{ice} (%)	S_{sw} (g kg ⁻¹)	A (μmol kg ⁻¹)
Bootstrap Avg.	84	15	0.61	0.57	35.01	0.82
Bootstrap 95% CI	[82, 87]	[13, 17]	[0.5, 0.7]	[0.2, 0.9]	[34.9, 35.2]	[0.0, 5.7]

Equation 8 can be expanded using the same terms as above. Q_{ice} in Equation 8 is substituted by rearranging Equation 7 and recognizing that $\rho_w V_w = \rho_{ice} V_{ice}$ in Equation 7. Dividing through by $\rho_w V_w c_{p,sw}$ yields:

$$T_{obs} = f_{sw} T_{sw} - \frac{\rho_{ice}}{\rho_w} f_{ice} T_{sw} + 0.167 \frac{\rho_{ice}}{\rho_w} f_{ice} \frac{L_f}{c_{p,sw}} + f_{cdw} T_{cdw} + f_{gmw} T_{gmw} \quad (9)$$

Based upon the observational results of Thompson et al. (2020) the addition of latent heat during sea ice formation is diminished by the factor of 0.167.

In summary, we can write versions of Equation 5 for each of the five noble gases, as well as temperature and salinity. The conservation of water provides one additional constraint yielding a total of 8 equations on 6 free parameters. The properties used to define the individual water types in the NGPT model are listed in Table 1. To estimate the uncertainty on model outputs, we used a Monte Carlo analysis (Press et al., 2007) to sample the distribution of input parameters to the mNGPT model, which in-turn was used to generate a non-parametric distribution of each fit parameter for each noble gas sample. The noble gas duplicate precision and CTD instrument precision were used to perturb the mNGPT model parameters (Beaird et al., 2015; Loose et al., 2016). The average and 95% confidence intervals of each fit parameter from the Monte Carlo analysis are found in Table 2.

3. Results and Discussion

3.1. Noble Gas Saturation Anomalies

Figure 3 depicts the dissolved gas saturation anomaly (Δ_i), where the gas concentration is expressed as the deviation from equilibrium saturation (Hamme & Severinghaus, 2007); zero saturation anomaly reflects a water column in solubility equilibrium with the atmosphere, assuming 1 atm of sea level pressure for consistency with other studies. Against the background of air-sea exchange, glacial melt in the ocean produces large helium and neon excesses; up to 10.3% for helium in the Ross Sea (Figure 3b). Panels a and b depict the conditions in the Ross Sea coastal polynyas during the PIPERS expedition, whereas panel c showcases Weddell Sea data from profiles along 57°S, acquired further offshore in the Antarctic Circumpolar Current (Loose et al., 2016). These profiles from the Weddell Sea reveal the same general fractionation of noble gases based on atomic mass, but with an attenuated signal in the lighter gases, reflecting the distance from a coastal region that set the properties observed in the Ross Sea coastal polynyas. The deficits of Kr and Xe are most extreme in the RSP as compared with the TNBP, with Xe extending below -6%. The vertical average of Xe is $-5.2\% \pm 0.3\%$ in TNBP as compared to $-6.0\% \pm 0.4\%$ in RSP, which is consistent with a greater quantity of GMW in the RSP.

3.2. mNGPT Results

The average uncertainty on the mNGPT solution over the entire PIPERS noble gas data set is presented in Table 2. The 95% confidence intervals on each sample are graphed in Figure S1 of the Supporting Information S1, and an example distribution of the Monte Carlo resampling of the mNGPT solution with 1,000 iterations is shown in Figure S2 of the Supporting Information S1. The water mass fractions f_{sw} , f_{cdw} , and f_{gmw} as well as S_{sw} show very little variation within their confidence intervals; f_{ice} and A show considerably greater variation—with the fraction of water lost to sea ice, showing mean confidence intervals ranging between 0.2% and 0.9%. Likewise, excess air was nearly zero on average, but the mean confidence intervals ranged between 0 and 5.7 μmol kg⁻¹ (Figure S1 in Supporting Information S1).

Two additional sources of uncertainty in the model solution can arise from uncertainty in the values of κ_{iw} , the ice-water partition coefficient, and through uncertainty in the value of sea level pressure. A table of literature values for κ_{iw} can be found in Table S1 of the Supporting Information S1. Aside from Top et al. (1988), we found no estimates of κ_{iw} for krypton and xenon. Lacking an alternative, and recognizing that Top et al. (1988) determined similar values of κ_{iw} of Ar, Kr, and Xe, we used the ratio between κ_{iw} for Ar determined by Top and by Postlethwaite (2002) to downscale

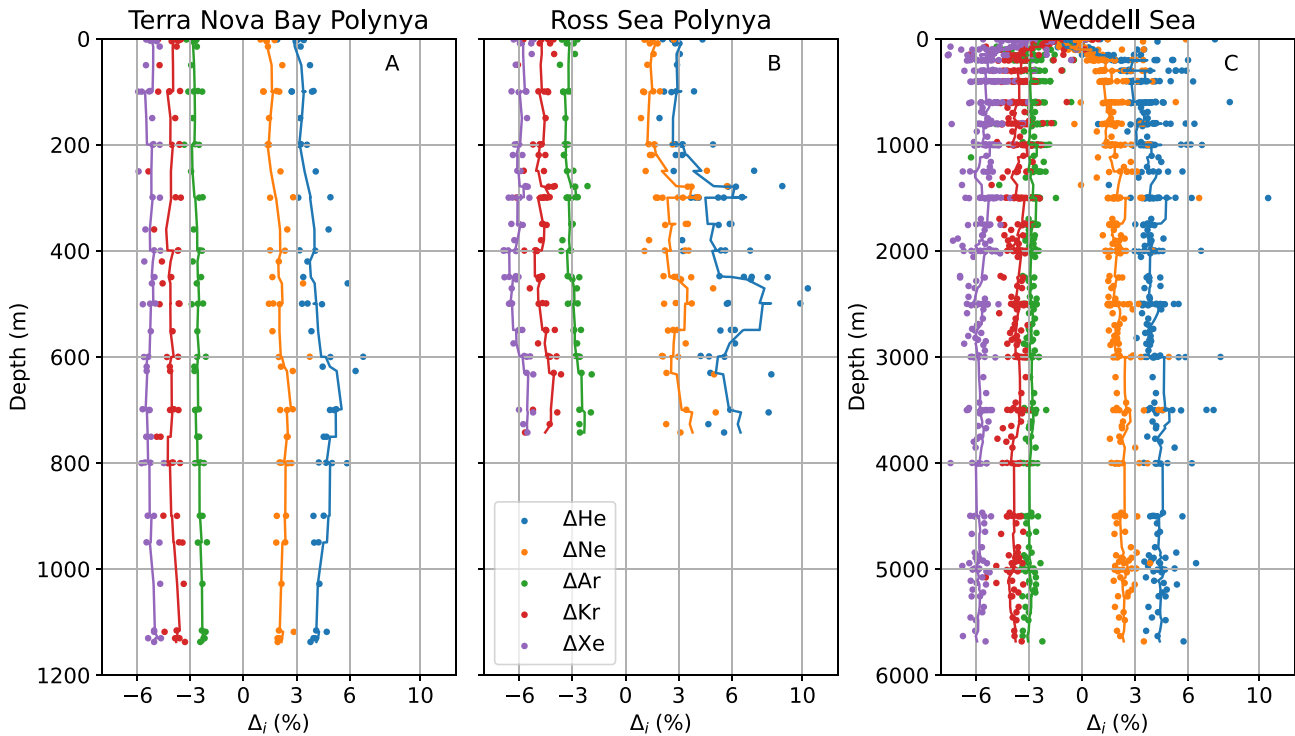


Figure 3. Saturation anomalies, $\Delta_i = (C_{\text{obs}}/C_{\text{eq}} - 1) \times 100$, where C_{obs} is the observed gas concentration and C_{eq} is the concentration in equilibrium with the atmosphere, for He, Ne, Ar, Kr, and Xe. Equilibrium solubility was determined using the solubility functions of Jenkins et al. (2019). Lines represent the 10-point rolling average of the individual anomalies for each gas. Saturation anomalies have been computed relative to 1 atm to make them comparable with anomalies from other studies and regions of the ocean.

the κ_{iw} values for Kr and Xe from those initially determined by Top. The reported values from Postlethwaite (2002) and the downscaled estimates for Kr and Xe are 1.22, 0.64, 0.15, 0.12, and 0.15 for He through Xe, respectively. When these are used in the mNGPT solution, the mean values of each parameter listed in Table 2 changed by less than 4% except A which decreased by two thirds to $0.26 \mu\text{mol kg}^{-1}$ and f_{ice} , which increased by roughly 10%–0.63%.

In Section 2.2 we reported sea level pressure as 0.9719 ± 0.0036 atm. If this standard deviation is incorporated into the solution, it has a similar magnitude change as κ_{iw} . The mean of parameters from the NGPT change by less than 2%, with greatest sensitivity manifesting in a 15% decrease in A and a 15% decrease in f_{ice} from the corresponding increase in sea level pressure. This sensitivity in A and f_{ice} is consistent with the results from the Monte Carlo analysis, but also well within the confidence envelopes that were described by that analysis (Figure S1 in Supporting Information S1).

Figure 4 depicts the six outputs from the NGPT model: f_{sw} , f_{cdw} , f_{gmw} , f_{ice} , S_{sw} , and Air injection together with the in-situ temperature and salinity. The profile plots in Figure 4, capture an appreciable amount of scatter in model outputs at each depth; much of this scatter can be attributed to real horizontal variations in the model parameter, which can be observed within the section plots in Figures 5–7. For example, Figure 5 shows that the purest remnant of CDW is found along the 27.76 isopycnal, between 175 and 177°E, and the largest concentrations of f_{ice} are found in the center of the TNBP near 165°E, but the values of f_{ice} diminish at stations adjacent to the Drygalski ice tongue (Figure 1), and further north in the polynya. Shelf Water is the predominant water property reflected in these late fall profiles; in the TNBP SW is vertically uniform near 87% of the water column. In the RSP, SW is ca. 82%, with the exception of a broad region between 200 and 600 m, where the SW distribution decreases to a minimum of 69%. This mid-depth region in the RSP is the primary area where the intrusion of modified CDW can still be identified. CDW reaches a maximum of nearly 30% by mass at 300 m.

The water properties revealed by the NGPT highlight the apparent differences between the two polynyas in 2017. The water column in the RSP contained a broad distribution of GMW between 300 and 600 m (Figure 4), and the remnants of a CDW intrusion were apparent along the potential density anomaly of $\sigma_{\theta} = 27.76$ (Figure 5). Overall the RSP was more stratified than the TNBP with density stratification reaching within 250 m from the ocean surface. The potential density contours reveal observably less buoyancy loss in the water column as compared

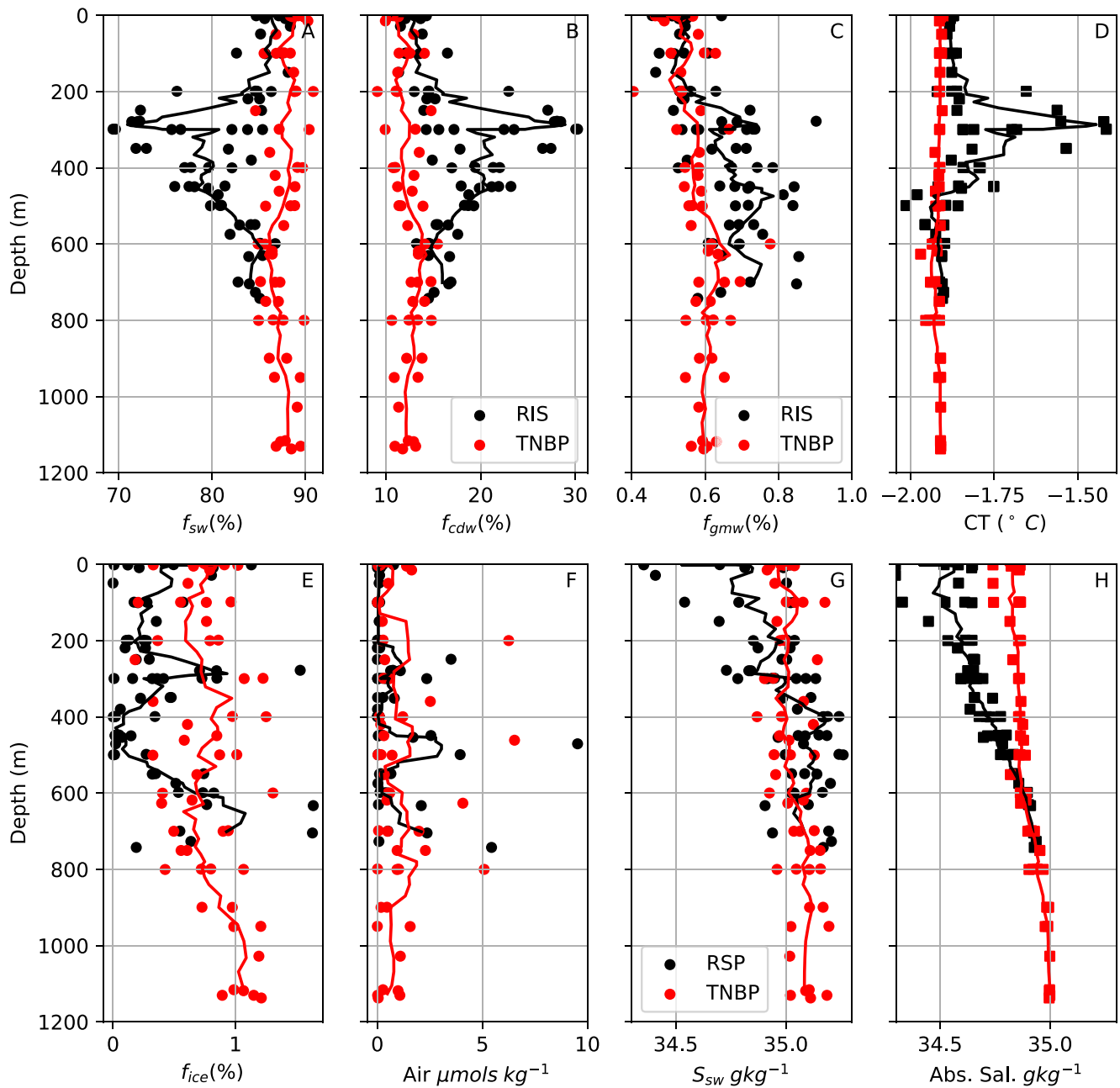


Figure 4. Scatter plots of the noble gas paleothermometer model result in panels (a–c) and (e–g) within the Terra Nova Bay and Ross Ice Shelf Polynyas. The solid lines indicate a 10-point vertical running average of the scatter points.

to the TNBP (Figure 5); potential density anomalies at the air-sea interface within the open water section of the TNBP were also heavier as $\sigma_{\theta} = 27.92$ as compared with $\sigma_{\theta} = 27.76$ in the RSP. However, we did not observe mixed layers that extended to the ocean bottom in either polynya as they presumably would after a full season of DSW formation. Figures S3 and S4 in Supporting Information S1 show individual noble gas profiles from the TNBP and RSP, together with the profile of in situ T and S and GMW, which reveal the mixed layers and stratified layers, as well as the interaction between the noble gas profiles and the resulting GMW profiles.

3.3. Glacial Meltwater Distributions

GMW in the RSP is sourced from the melting of the Ross Ice Shelf, and associated with CDW intrusions, but is known to exit the ice shelf cavity as confined outflows (Loose et al., 2009; Smethie & Jacobs, 2005). The intrusion

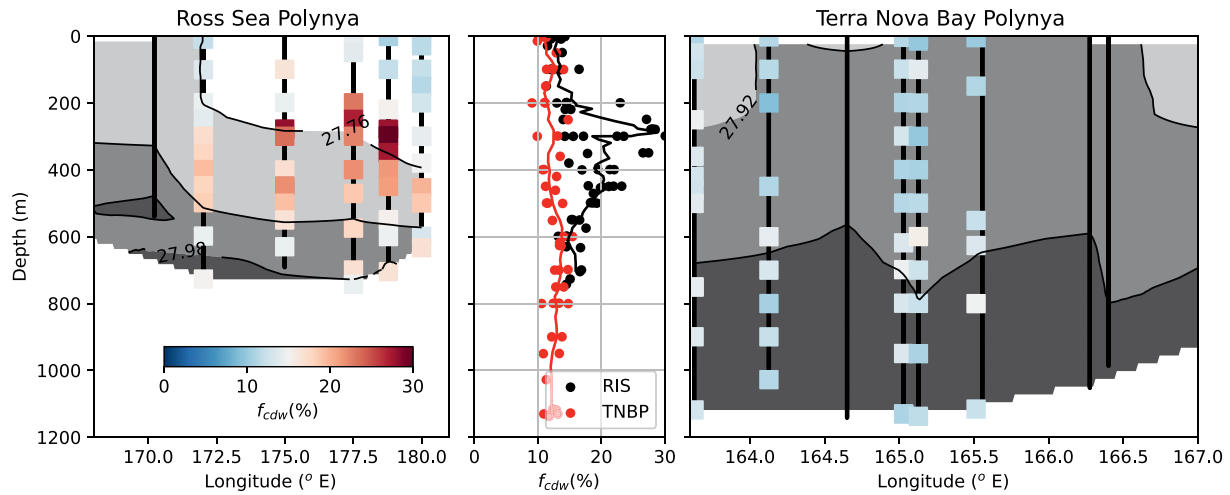


Figure 5. A spatial breakout of the Circumpolar Deep Water distribution in the Ross Sea and Terra Nova Bay polynyas. The gray shading and black contour lines are the potential density anomaly (σ_θ), computed using absolute salinity and conservative temperature.

of CDW near 300 m in the RSP (Figure 5) is also associated with one of two extrusions of GMW (Figure 6). The most prominent appears at 300 m, coinciding with the temperature maximum. This feature of elevated meltwater is found near the dateline at 180° and is known as the furthest west extrusion of GMW from under the ice shelf. The extrusion of GMW between 500 and 600 m may be associated with DSW and the production of ice SW with temperatures below -2°C (Loose et al., 2009; Smethie & Jacobs, 2005). In addition to the local production of GMW, the RSP profiles likely also reflect meltwater import from upstream in the Amundsen and Bellingshausen seas, especially near the surface with transport via the Antarctic Coastal Current.

The meltwater distribution in TNBP is relatively more uniform with lower content than what is found in the RSP; the mean meltwater content in the RSP is 0.64% versus 0.57% in the TNBP, although these differences are within the 1σ uncertainty of each other. The meltwater content found in TNBP is likely associated with melting at the base and edges of the Drygalski Ice Tongue as well as from the Hells Gate and Nansen ice shelves (Frezzotti, 1993).

3.4. Sea Ice Fraction Distributions

The vertical distribution of f_{ice} reveals the differences in seasonal evolution between the RSP and TNBP in 2017 (Figure 7). As we reported in Section 3.2 the mixed-layer depth was significantly shallower in the Ross Sea—reaching

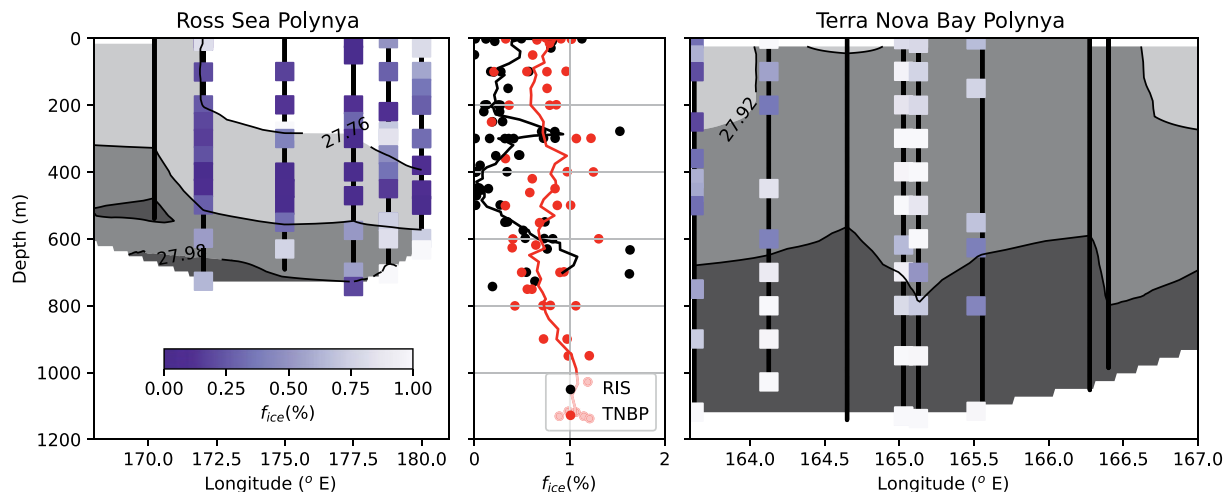


Figure 6. A spatial breakout of the Glacial Meltwater distribution in the Ross Sea and Terra Nova Bay polynyas. The highest meltwater concentrations in the Ross Ice Shelf Polynya coincide with the highest quantity of Circumpolar Deep Water, near 300 m. The gray shading and black contour lines are the potential density anomaly (σ_θ), computed using absolute salinity and conservative temperature.

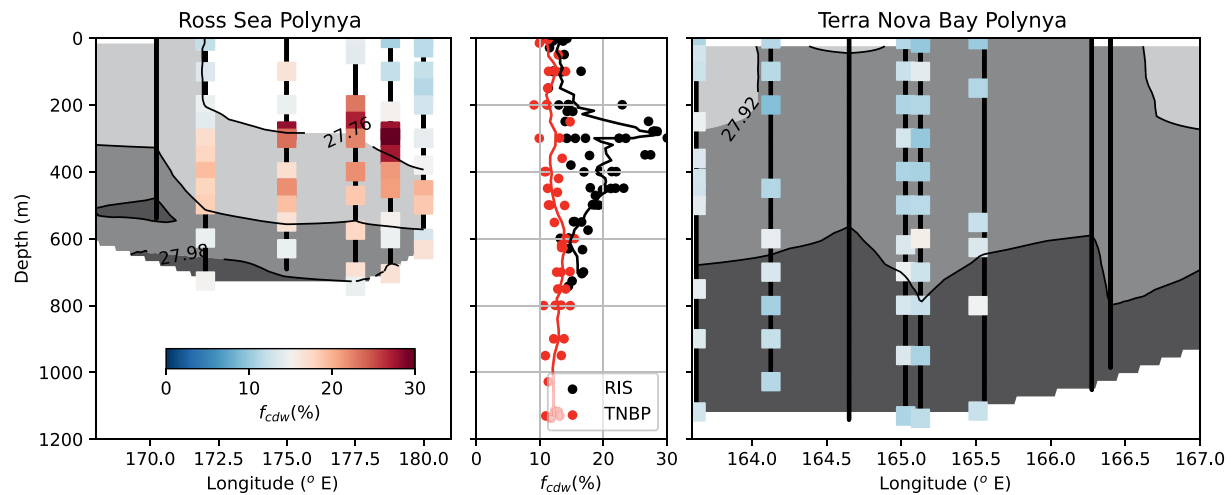


Figure 7. A spatial breakout of the percentage of seawater removed as sea ice (f_{ice}) within the Ross Sea and Terra Nova Bay polynyas. The profiles reveal highest f_{ice} concentrations in the deepest portion of the TNBP mixed layer, near 165°E. The gray shading and black contour lines are the potential density anomaly (σ_θ), computed using absolute salinity and conservative temperature.

an average depth of 250 m, compared to 650 m in the central part of the TNBP. In this circumstance, we will interpret the values of f_{ice} separately from within and below the mixed-layer, because they effectively represent two different years. The f_{ice} values beneath the mixed layer are a remnant of the integrated sea ice melt from the 2016 freeze season, provided the polynya mixes to the bottom during winter. By the same mechanism, the mixed-layer f_{ice} values represent ice formation from the 2017 freeze season. In the upper 250 m of the RSP, the average f_{ice} was 0.37%; between 250 m and the bottom of the RSP profiles at 800 m, the average f_{ice} was 0.75% (Table 3). In comparison, the average of f_{ice} within the mixed-layer of TNB was 0.72%. Below 650 m, this value increased to an average of 0.89%. That is, the values of f_{ice} were more than 50% less in RSP mixed-layer in 2017 compared to the TNBP mixed-layer. This coincides with a big difference in wind speed for these two regions: In 2017, the automated weather station data from the edge of the Ross Ice Shelf (Station Vito) showed a mean wind speed of 5.7 m s⁻¹ between April and October. During the same period, the mean wind speed at the nearest automated weather station Terra Nova Bay (TNB) was 20.3 m s⁻¹.

In the RSP during 2017/2016, ice production reached 0.9/6.0 m of ice and in TNBP, ice production was 4.7/11.6 m of ice. To obtain the 2017 estimates we multiplied the depth of the mixing column in 2017 by f_{ice} ; to obtain the ice production in 2016, we multiplied the mean value of f_{ice} found below the mixing column by the full depth of the water column—800 and 1,300 m for the RSP and TNBP respectively. This invokes the assumption that the values below the mixed-layer are a record of the *entire* water column f_{ice} fractions during the previous winter, when

Table 3

Estimates of the Annual Ice Production in Meters, and the Seasonal Average Ice Production in cm d⁻¹, for the Ross Ice Shelf Polynya and Terra Nova Bay Polynya Using the Mixed-Layer Depths and the Vertical Average of f_{ice} Within the Mixed-Layer for 2017 and Beneath the Mixed-Layer for 2016

This study	f_{ice} (%)	Column depth (m)	Seasonal average (cm d ⁻¹)	Annual ice production (m)
RSP, this study, 2016	0.75 ± 0.23	800	2.8 ± 0.87	6.0 ± 1.9
RSP, this study, 2017	0.37 ± 0.11	250	1.1 ± 0.35	2.35 ± 0.72
RSP, Ohshima et al. (2016)	AMSR-E radiometer, thin ice algorithm		3.5	–
RSP, Petrelli et al. (2008)	Ocean model		7.0	–
TNBP, this study, 2016	0.89 ± 0.28	1,300	5.4 ± 1.7	11.6 ± 3.6
TNBP, this study, 2017	0.72 ± 0.22	650	6.5 ± 2.0	13.9 ± 4.3
TNBP, Schick (2018)	Heat budget		–	27
TNBP, Petrelli et al. (2008)	Ocean model		7.7–11.0	–
TNBP, Ohshima et al. (2016)	AMSR-E radiometer, thin ice algorithm		3.9	–

Note. The uncertainty was determined as 1 σ of the f_{ice} population from bootstrap resampling. In addition, Table 2 lists the prior ice production estimates and their associated estimation methods.

the polynyas last mixed to the bottom. For comparison purposes, these annual ice production estimates can be converted to average daily ice production rates for the season of freezing. Remote sensing estimates of ice production use the period from March to October or 214 days to capture the freezing period (Ohshima et al., 2016), so we have divided the total ice production by this duration in the 2016 calculations. For the 2017 calculations, PIPERS measurements occurred in the TNBP between 1 and 11 May or approximately 72 days into the freeze season, and between 16 and 21 May in the RSP, 82 days into the freeze season. This suggests an ice production rate of 1.1 cm d⁻¹ for the RSP and 6.5 cm d⁻¹ in the TNBP by mid-May in 2017 (Table 2). If the same rate of ice production persisted throughout the freezing season, it would be equivalent to 2.4 m of ice production in the RSP and 13.9 m ice production in the TNBP during 2017. Because these measurements likely took place during the seasonal progression of mixed-layer deepening, convection may have the effect of mixing the previous year's noble gas fingerprint into the mixed layer where it is not entirely re-equilibrated. In that regard, the estimates of ice production made for 2017 are not entirely independent of the remnant from prior years.

These values suggest that the seasonal ice production rate per unit area is 1.9 times greater in TNBP in 2016 and 5.8 times greater in 2017 than in the RSP (while noting that the water column values of f_{ice} in 2017 only capture the first one third of the 2017 freezing season). Petrelli et al. (2008) report a production rate in TNBP that is 1.6 times that of the RSP. In 2017, the wind speeds in TNBP were 3.5 times higher than in the RSP; when considering that heat loss is proportional to the square of the wind speed, it is perhaps not unreasonable to expect so much more sea ice production in TNB under these conditions in 2017.

The values of ice production fall at the low end of the range of previous estimates of annual ice growth in TNBP, although the estimates of ice growth from 2017 for the RSP are lower than most previous estimates in the literature. An analysis of ice production by Schick (2018) estimated the spatial gradient in air-sea heat fluxes along an upstream-downstream axis in the TNBP using a series of unmanned aerial system flights collected in 2009 and 2012. These spatial gradients were merged with 7 years of Automated Weather Station data to develop a winter climatology of heat flux and ice production. Overall, these estimates reveal 3–5 m of ice production per month between April and October or an average of 27 m in annual ice production, which is larger by a factor of 1.9–2.3x than our 2016 and 2017 estimates. Petrelli et al. (2008) simulated a strong and a weak winter in TNB and a strong winter in RSP. The strong and weak winters in TNB produced seasonal averages of 7.7 up to 11.0 cm d⁻¹, which are greater than our estimates for 2016 and 2017 in TNBP. In the RSP, a winter of intense ice formation yielded 7.0 cm d⁻¹, which is 2.5–7x greater than what these water column estimates produced (Table 3). Remote sensing algorithms, for example, Ohshima et al. (2016) produced mean estimates over 9 winters to yield 3.5 cm d⁻¹ for the RSP and 3.9 cm d⁻¹ for the TNBP using the thin ice algorithm for AMSR-E developed by Nihashi and Ohshima (2015). These are closest to our estimates in the RSP, but are only about 50%–70% of our estimates of in TNBP. However, these algorithms have been modified to detect frazil ice formation and this change has significantly increased the estimates of annual ice production to greater than 20 m yr⁻¹, including in TNB (Nakata et al., 2021). Last, we note that two PIPERS-related studies of TNBP have invoked the potential for sea spray to enhance heat loss (Guest, 2021) and sea ice production, perhaps by as much as 40%, at least within the open water areas of the polynya. While there were no direct measurements of sea spray during PIPERS, wave buoy estimates of mean square slope suggest some waves were steep enough to experience breaking and production of sea spray (Ackley et al., 2022). It remains difficult to determine what portion of the polynya is open water and what portion is frazil ice-covered water, during katabatic wind events; results from Nakata et al. (2021) and the rapid decrease in atmospheric heat flux suggest some open water may extend as far as 25–30 km from the coast in both the RSP and TNBP, which is a relatively narrow region compared to the overall polynya area.

These are some of the first estimates of ice production using water column measurements of dissolved gas tracers. The results fall at the low the range of prior production estimates for these same polynyas; if sea spray is an important ice production mechanism, this would likely not appear in the water column noble gas fingerprint of ice production, which might explain why these values are low. Another explanation may be the use of an overly conservative value for the ice/water partition coefficient (κ_{iw}), which is likely to be greater for frazil ice (see Section 5). For our purposes, the evidence of a sea ice production signal in the noble gases is sufficient motivation to support the further interpretation of the f_{ice} fractions in terms of their role on the solubility pump.

3.5. Air Bubble Injection

The air content in both polynyas was lower than expected (Figure 4f): the average air content injected was 0.9 $\mu\text{mol kg}^{-1}$ in TNBP and 0.7 $\mu\text{mol kg}^{-1}$ in RSP, although there is a high degree of variation in the individual

estimates from the mNGPT model (Figure S1 in Supporting Information S1). Within both polynyas there is not a lot of discernable structure to the air bubble profiles, and indeed the values are indistinguishable from zero within the confidence intervals (Table 2).

There have been several model and data-based evaluations of air bubble injection in the ocean. Several previous studies have computed bubble injection fluxes that translate to between 1.2% and 2.5% excess argon on average between 1,000 and 5,000 m (Liang et al., 2013; Nicholson et al., 2011; Stanley, Jenkins, et al., 2009). Because air injection results in quantitative dissolution of gases at the mixing ratios for the atmosphere, these argon excesses translate to between 26 and 44 $\mu\text{mol kg}^{-1}$ of excess air from bubble injection. Therefore, the air bubble content in these Ross Sea Polynyas is 2%–3% of the global estimates.

These low values of air injection seem even less congruous when we consider the influence of katabatic winds ranging from 16 to 27 m s^{-1} during the period of PIPERS field data collection in TNB. One large eddy simulation model study of air bubble injection reveals that winds above 20 m s^{-1} resulted in excess argon saturation up to 6% (see Figure 3 in Liang et al., 2013) or 105 $\mu\text{mol kg}^{-1}$ suggesting the estimated values of air bubble injection might be as small as 1% of the expected open ocean value for these forcing conditions.

The explanation for such a strong limitation in air bubble injection is most likely tied to frazil ice production and accumulation of crystals in the surface layer. Frazil ice, or disaggregated ice crystals in seawater can reach concentrations where the interactions between fluids and the suspended particles changes the rheology of the flow (Ayel et al., 2003; Matsumura & Ohshima, 2015). These types of fluids are referred to as two-phase flows, analogous to slurries composed of sediment and water. Such were the conditions we found, particularly in the TNBP, which was extensively covered by frazil ice. Model studies of Matsumura and Ohshima (2015) reveal that frazil ice concentrations of up to 100 g of ice per m^3 can exist to depths of 30 m or greater in the surface ocean. These results match the observations of Thompson et al. (2020) who attributed heat and salt anomalies between 10 and 50 m below the water surface to frazil ice production during the PIPERS expedition. As turbulence is attenuated, the crystals will migrate buoyantly to the surface to become incorporated into a consolidated ice pack. The visible imagery recorded in TNB during PIPERS shows that at the surface, the frazil ice is organized into wind rows, likely a consequence of Langmuir cells (Ackley et al., 2020; Thompson et al., 2020). This can be explained in part by the increase in viscosity: using the ice-dependent viscosity equation from Matsumura and Ohshima (2015), water viscosity increases by nearly 40% for every 10% increase in frazil ice fraction (see Figure S5 in Supporting Information S1). These changes in viscosity also imply a decrease in the diffusive gas transfer velocity with a reduction in gas transfer velocity (k) of 20% for every 10% increase in frazil ice; thus comparatively less gas will enter the water by turbulent diffusion. As the frazil crystals migrate buoyantly toward the surface ocean, they produce a surface layer that is elastic with respect to ocean waves, but with a significant increase in surface tension that limits breaking and bubble entrainment. Lab and field studies by Martin and Kauffman (1981) illustrate rapid decays in surface gravity wave amplitude, and the same phenomenon influences wave breaking as wave steepness is quickly attenuated (Ackley et al., 2022). In this environment, all types of air-sea gas exchange are suppressed; air bubble injection appears to be strongly limited because of its dependence on breakage of the water surface.

While we assert that there are several lines of physical evidence to support a suppression in air bubble injection, it is worth recalling that we noted in Section 3.3 that two other PIPERS studies suggest sea spray production by wave tearing may have been important to air-sea heat flux (Guest, 2021) and ice production. These are the sort of conditions often associated with air bubble injection, which appears to contradict our results. While there were no direct measurements of sea spray during PIPERS, wave buoy estimates of mean square slope suggest some waves were steep enough to experience breaking and production of sea spray (Ackley et al., 2022). The net effect of open water bubble injection depends on the polynya surface area that is free of frazil and consolidated ice. It remains difficult to determine what portion of the polynya is open water and what portion is frazil ice-covered water during katabatic wind events; results from Nakata et al. (2021) and the rapid decrease in atmospheric heat flux, suggest some open water may extend as far as 25–30 km from the coast in both the RSP and TNBP, which is a relatively narrow region compared to the overall polynya area.

3.6. Diffusive Air-Sea Exchange in the mNGPT

The role of diffusive air-sea gas exchange, which arises from a gas partial pressure disequilibrium between the air and sea, is an important component to setting the properties of deep water that form in both the northern and

southern hemisphere, and may indeed be the dominant process leading to deep noble gas disequilibria (Hamme et al., 2017; Nicholson et al., 2010; Seltzer et al., 2019), especially in formation regions where ice does not form or melt. Within the mNGPT, diffusive gas exchange is indirectly represented in two ways: (a) through the transformation of unventilated CDW into SW, which takes place heuristically through convection, cooling and air-sea interaction which is reflected in their end member properties (Table 1) and (b) by using S_{sw} as a free parameter that varies iteratively and tunes the gas solubility $\beta(S_{sw}, T)$ of Shelf Water (f_{sw}) (Equation 5). We will discuss how these two combine to yield an estimate of the diffusive gas exchange from the mNGPT.

Within the mNGPT, CDW is defined by its subsurface properties, which have been identified offshore at the continental shelf break, and are known to enter the continental shelf and become ventilated as described in the Introduction. Therefore, any non-zero fraction of CDW (f_{cdw}) represents a remnant of this subsurface water mass, which has not had its properties completely reset by ventilation. The mNGPT solution finds an average $f_{cdw} = 12\%$ in the TNBP, demonstrating that a remnant of CDW has been recorded by the noble gases, which is distinguishable from the fraction of SW and the effect of sea ice, glacial melt, and air bubbles. Following the assumptions of the mNGPT model, the diffusive gas exchange can be estimated by observing the transformation of CDW into SW: Starting from the CDW end member, we can express the contribution to ventilation, expressed as a concentration:

$$C_{g-e} = (f_{sw}\beta(S_{sw}, T) + f_{cdw}C_{cdw}) - f_{tot}C_{cdw} \quad (10)$$

Here, the RHS term in parentheses represents the non-freshwater components of the mNGPT solution, and $f_{tot}C_{cdw}$ represents subsurface CDW before it is transformed to SW. Because $f_{tot} = 1 \sim f_{sw} + f_{cdw}$, the relationship can simplify to:

$$C_{g-e} = f_{sw}(\beta(S_{sw}, T) - C_{cdw}) \quad (11)$$

Equation 11 also demonstrates how the free parameter S_{sw} can adjust to the influence of diffusive gas exchange by determining the gas solubility of Shelf Water (see Equation 5). This permits the model to select for a SW gas concentration that is determined not by the in situ hydrographic conditions, but rather by the physical conditions recorded by the noble gases. The mNGPT yielded profile shapes of S_{sw} that are largely in agreement with the in-situ salinity profiles, within both polynyas (see panels g and h, Figure 4). In situ salinity is nearly isohaline above 600 m in TNBP. In contrast, there is a progressive salinity decrease from deep to shallow depths in the Ross Sea, reflecting ambient stratification in the RSP at this stage in the season. These same patterns are more or less reflected in S_{sw} , although S_{sw} was on average 0.3 g kg^{-1} saltier in the RSP and 0.14 g kg^{-1} saltier in the TNBP. This has the effect of reducing the gas holding capacity of SW, which moves the solution further away from complete ventilation. For Kr, the reduction in solubility is $-5.0 \times 10^{-6} \text{ } \mu\text{mol kg}^{-1}$ in the TNBP. This reduction is equivalent to a decrease in the saturation anomaly of -0.13% .

As an example of the ventilation by diffusive gas exchange, we can apply Equation 11 to the mean water column values in TNB. Referring to Table 1, the Kr concentration in CDW is $3.91 \times 10^{-3} \text{ } \mu\text{mol kg}^{-1}$, Kr concentration in SW is $4.34 \times 10^{-3} \text{ } \mu\text{mol kg}^{-1}$, and the average of f_{sw} is 88%. These numbers in Equation 11 yield an increase in krypton content by $3.91 \times 10^{-4} \text{ } \mu\text{mol kg}^{-1}$, which is 9% of the mean krypton concentration observed in TNB. This result is further developed in Section 4, below. The results highlight the important role that diffusive gas exchange plays in determining the gas properties of SW, even as gas exchange is reduced by sea ice cover (Bigdeli et al., 2017; Takahashi et al., 2009).

4. The Physical Processes Setting Deep Water Solubility Conditions

Referring to the schematic model described in (Figure 2), the water in the Ross Sea is primarily composed of CDW that crosses the continental shelf break and becomes ventilated via surface and ice processes. This modified water mass receives inputs from glacial and sea ice melt, although precipitation as snow may contribute in some coastal seas. During the modification process, CDW cools and freshens, especially as it becomes modified during winter heat loss in polynyas, the temperature decreases to below the freezing point or -1.95°C as observed in the mixed-layer, during the PIPERS expedition. This cooling increases the capacity of this water to absorb gas, and that is reflected in the saturation anomalies depicted in Figure 3. At the same time, the extreme surface cooling is attended by sea ice formation and vigorous turbulence that may lead to air-sea gas exchange by bubbles and by diffusion.

To illustrate the impact of ice processes and air-sea processes on the solubility pump, we seek to reconstruct the gas budget within the Ross and Terra Nova Bay polynyas (Figure 8). Ne, Ar, and Kr are used in Figure 8 to illustrate differences that arise, based on the differences in molecular properties of the light and heavy noble gases. To reconstruct the gas budgets we use the outputs of the mNGPT solution—effectively rearranging the terms in Equation 5 to show each relative contribution. Old circumpolar water enters the Ross Sea with a dissolved Ar content of $16.2 \mu\text{mol kg}^{-1}$ before it is ventilated. This water is represented as “unventilated CDW” in Figure 8. At the time of the PIPERS observations, the in situ Ar concentration was $17.7 \mu\text{mol kg}^{-1}$, an increase of $1.5 \mu\text{mol kg}^{-1}$ in Ar compared to CDW. Ice processes—GMW intrusion and sea ice formation—are both sources of dissolved Ar to the water column: GMW restored Ar to the water column, contributing 18% ($0.27 \mu\text{mol kg}^{-1}$) to the net Ar ventilation in TNBP. Sea ice formation added an additional 5.9% to Ar ventilation and air bubble injection contributed the least at 0.54%. Last, diffusive gas exchange contributed the largest amount, increasing Ar by $1.14 \mu\text{mol kg}^{-1}$ in TNBP, which is 76% of the ventilation budget. The last term, the diffusive ventilation is not an explicit output from the mNGPT model but was determined using the procedure described above in Section 3.6 and Equation 11. Table S2 in Supporting Information S1 presents the average breakdown of the ventilation budget for Ne, Ar, and Kr that are graphed in Figure 8.

For a more soluble noble gas like krypton, diffusive gas exchange accounts for the preponderance of ventilation, or 91% in TNB. Glacial melt, sea ice formation, and air bubble injection restored 7.3%, 4.1%, and 0.2% respectively. The fact that these percentages sum to 102.6% reflects the uncertainty in the ventilation budget reconstruction. A visual depiction of the uncertainty can be seen in Figure 8, by comparing the solid and dashed black lines in each panel. Neon has a low seawater solubility compared to argon and krypton, and its concentration in glacial ice dominates the neon budget. Glacial melt added $5.0 \times 10^{-4} \mu\text{mol kg}^{-1}$ of neon to the polynya water, equivalent to 131% of the net gas ventilation, while sea ice formation and air bubble injection increased dissolved neon by a modest 2.9% and 3.7% of the ventilation budget, respectively. As the in-situ saturation anomaly, ΔNe , is greater than zero, diffusive gas exchange leads to neon evasion to the air and a reduction in the neon concentration, equivalent to -19.0% of the ventilation budget. This also reveals a budget closure misfit of 18% for neon (Figure 8).

Collectively, these results depict how ice processes, in addition to air-sea gas exchange can have an appreciable impact on the gas budget of polynya waters and therefore on DSW. The total ventilation of the most soluble noble gases (Kr, Xe) are heavily influenced by diffusive gas exchange ($\sim 90\%$ of ventilation), while ice processes accounted for the other ($10\% \pm 2.6\%$). However, the balance shifts for moderate (Ar) and low (Ne) solubility gases. Ice processes accounted for $24\% \pm 0.6\%$ of net argon ventilation and $134\% \pm 18\%$ of the net neon ventilated. In the case of every gas, the ventilation of polynya water by air bubble injection appeared to be negligible. They also affirm that the diffusive gas exchange is the leading term in ventilation within polynyas, except perhaps in special cases like He and Ne—gases that have a relatively high concentration in air (and thus in glacial ice) as well as low solubility in water. Throughout the global ocean, neon excesses are thought to be caused by air bubble injection (Stanley, Jenkins, et al., 2009), but we have observed this process is suppressed in polynyas. Of course, the influences of ice on deep water properties do not occur at deep water formation sites that are further north in the Southern Ocean, nor to the formation of deep water in the northern hemisphere.

These results can hopefully clarify an apparent misunderstanding that has entered the ocean noble gas literature on the use of the NGPT to study deep ocean ventilation. Loose et al. (2016) used results from the NGPT to reveal the role that ice processes could play in setting gas properties in deep water; this application of the NGPT model was interpreted by Hamme et al. (2017) as having arisen by neglecting diffusive gas exchange within the NGPT. A subsequent study (Seltzer et al., 2019) has presented these as competing hypotheses, where ice (Loose et al., 2016) versus temperature-dependent diffusive gas exchange (Hamme & Severinghaus, 2007; Hamme et al., 2017) control deep water ventilation. However, both processes can take place in polynyas, and while the NGPT does not have a specific temperature dependent gas disequilibrium term, it is capable of permitting gas disequilibrium by letting salinity of SW vary as a free parameter and thereby control the gas concentration. This is in fact the conceptual insight that led to the development of the paleothermometer—a recognition that the gas content in the water does not necessarily reflect the in situ conditions, but instead is a weighted time-average of the temperature at the air-water interface (Aeschbach-Hertig & Solomon, 2013).

Finally, it is important to acknowledge the limitations of a model such as the mNGPT. First, the control of salinity on solubility is an imperfect proxy for the kinetic fractionation of gas exchange so that when the mNGPT solution is optimized for all five noble gases, it can lead to a small bias in the gases that equilibrate faster of up to 1% for

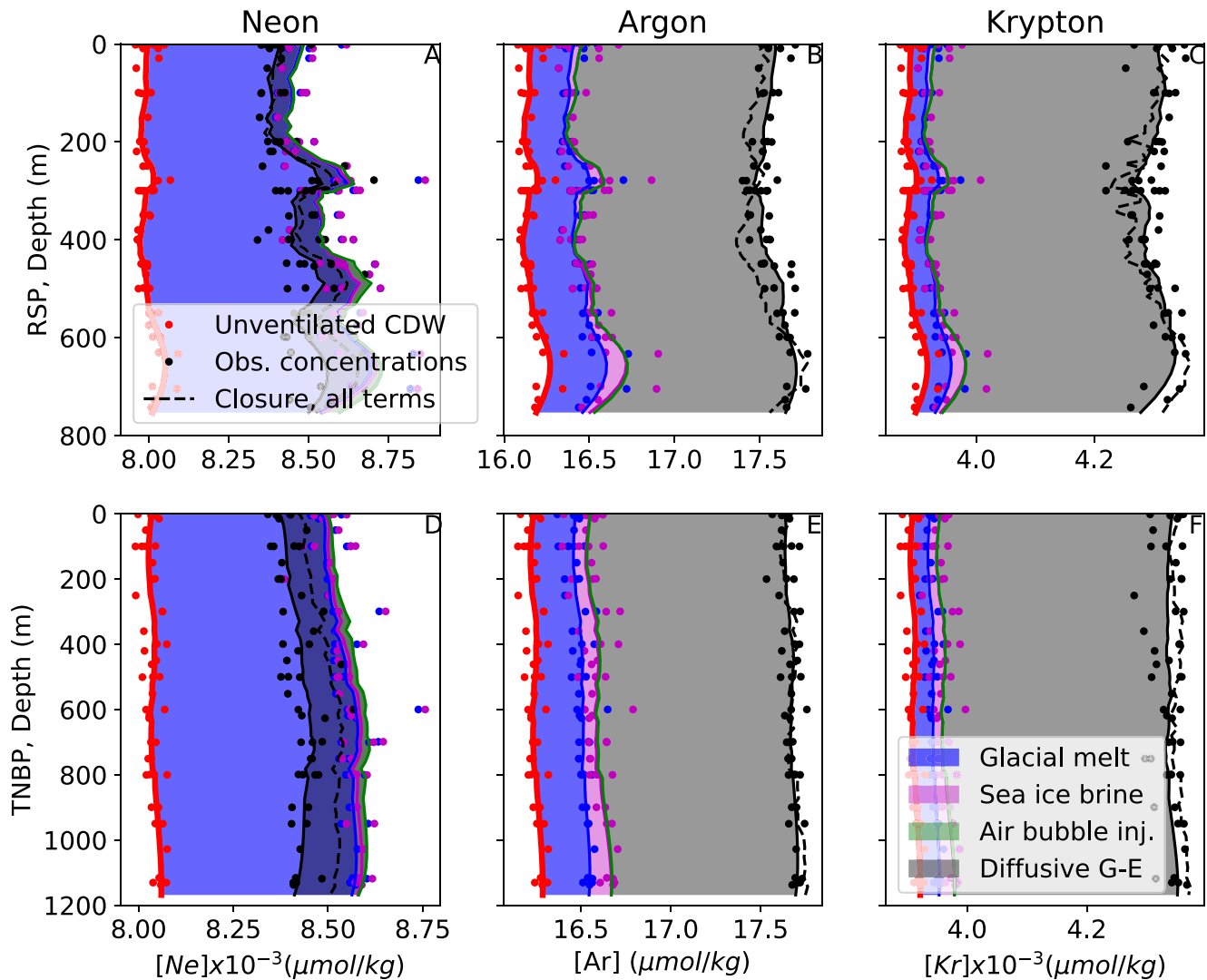


Figure 8. A reconstruction of the contribution of ice and air-sea processes to the gas ventilation of Circumpolar Deep Water, as it is transformed into Dense Shelf Water in polynyas: The areas shaded by color represent the contribution of each process to the restoration of the gas (Ne, Ar, Kr) saturation within the observed polynya water, including glacial melt (blue), sea ice brine (magenta), air bubble injection (green), and diffusive gas exchange (gray). The darker blue shading in the Ne plot (overlap of blue and gray) is caused by the nonmonotonic increase in Ne due to glacial melt and decrease in Ne due to diffusive gas exchange. Solid black line is a running average of the observations in black circles. The black dashed line represents the sum of all terms the reconstruction and should align with the observations. The top row depicts the water column in the Ross Ice Shelf Polynya, The bottom panel reveals the same in the Terra Nova Bay Polynya.

He and 0.7% for Ne. We did not see evidence of kinetic fractionation following a gas exchange pattern. Next, the model is non-linear in the first two terms on the RHS of Equation 5, which can potentially capture feedback between free parameters, such as for example, air bubble content (A) and the net fraction of SW (f_{sw}). Taking the product of two free parameters can result in poorly constrained error minimization, although the Monte Carlo analysis should reveal those weaknesses, expressed in the confidence intervals around each parameter. In general, we have sought to minimize the introduction of nonlinear terms in the mNGPT as they can lead to possible overfitting by the model. The mNGPT model can be thought of as a steady-state model that is attempting to represent highly transient seasonal processes, such as convection and sea ice formation. Another way to state this is that, the noble gases tend to integrate the influence of each physical process since the prior seasonal maximum or minimum, or over the residence time of the water mass. The seasonal cooling and progressive convection in these polynyas represent a secular evolution since the summer maximum in water temperature and stratification. It is not unreasonable to expect that if the PIPERS expedition had returned a month later, the remnant of CDW remaining in the water column would have been further ventilated, leading to a smaller f_{cdw} and larger f_{sw} .

Likewise, the values of f_{ice} would likely be greater as Kr and Xe accumulate in the water column and He and Ne escape to the atmosphere. In this regard, the mNGPT is a simplification of a highly dynamic process, but it is also capable of using the noble gas tracers to estimate the net progression of the physical processes that act on gas concentration.

5. Summary

These results reveal how physical processes stack up to restore the gas solubility deficit in DSW, as it forms during the extreme conditions that take place in latent heat polynyas during winter. Previous studies evaluating the impact of ice on the solubility pump have focused solely on how the sea ice cover acts to restrict the rate of air-sea gas exchange (Nicholson et al., 2010; Sigman et al., 2010; Stephens & Keeling, 2000; Toggweiler et al., 2003). In particular, Toggweiler et al. (2003) demonstrated how the reduction of the surface area of the southern outcrop of the MOC leads to an increase in the air-sea pCO_2 differential and therefore a decrease in the solubility pump. This work reveals that the sole focus on inhibition of air-sea gas exchange overlooks the additional ice-associated processes that also influence the restoration of gases in actively forming DSW, including sea-ice formation and GMW inputs. As we consider the implications of these results from the NGPT model, they suggest that the transport of dissolved solutes (both ions and gases) during ice freeze and melt cycling is significant to the determination of preformed gas properties in deep water that forms in ice-affected regions. By the same token, ice cover appears to eliminate the contribution of air bubble injection to the total air-sea gas exchange. Therefore, we need more detailed knowledge of how solubilized compounds in seawater behave when confronted with the freezing process. While sea ice formation had a relatively small role in total ventilation of gases (~6% for Ar and 4% for Kr), the formation was estimated using the equilibrium partition coefficients for the noble gases to parameterize how gas is separated between sea ice and water, which have been developed for more mature ice conditions. But polynyas form a wide spectrum of ice types including frazil and grease ice, which likely affect the way that gases are excluded into brine, and it is becoming apparent that frazil ice may be most associated with DSW formation (Nakata et al., 2021; Thompson et al., 2020; Tison et al., 2020). It is likely that as individual frazil ice crystals nucleate, the separation of gases is even more efficient than for mature columnar ice, favoring the deposition of solutes in the water column, but the behavior of dissolved ions and gases under these conditions is unknown. Biogenic gases such as O_2 and CO_2 require additional tools to distinguish between biological physical contributions. When considering CO_2 , a buffered gases, the role of sea ice could become even more interesting as cryogenic conditions are known to trap alkalinity in sea ice, while exporting dissolved inorganic carbon (Dieckmann et al., 2008). These effects can be addressed in future studies, because the noble gases provide a framework to estimate the physical processes that influence ventilation.

Data Availability Statement

The noble gas data is available at the US Antarctic Program Data Center (Loose, 2022, <https://doi.org/10.15784/601609>). Hydrographic data is available through the Marine Geoscience Data System (Ackley, 2017, <https://www.marine-geo.org/tools/search/entry.php?id=NBP1704>).

References

- Ackley, S. F. (2017). Polynyas, ice production and seasonal evolution in the Ross Sea [Dataset]. <https://doi.org/10.7284/907629>
- Ackley, S. F., Smith, M., Geste, P. S., Herman, A., & Shen, H. (2022). Winds, waves and ice formation in a coastal polynya. In *Proceedings of the 26th IAHR international symposium on ice*.
- Ackley, S. F., Stammerjohn, S., Maksym, T., Smith, M., Cassano, J., Guest, P., et al. (2020). Sea-ice production and air/ice/ocean/biogeochemistry interactions in the Ross Sea during the PIPERS 2017 autumn field campaign. *Annals of Glaciology*, 61(82), 181–195. <https://doi.org/10.1017/aog.2020.31>
- Aeschbach-Hertig, W., & Solomon, D. K. (2013). Noble gas thermometry in groundwater hydrology. In P. Burnard (Ed.), *The noble gases as geochemical tracers* (pp. 81–122). Springer Berlin Heidelberg.
- Allan, R., & Ansell, T. (2006). A new globally complete monthly historical gridded mean sea level pressure dataset (HadSLP2): 1850–2004. *Journal of Climate*, 19(22), 5816–5842. <https://doi.org/10.1175/JCLI3937.1>
- Ayel, V., Lottin, O., & Peerhossaini, H. (2003). Rheology, flow behavior and heat transfer of ice slurries: A review of the state of the art. *International Journal of Refrigeration*, 26(1), 95–107. [https://doi.org/10.1016/S0140-7007\(02\)00016-6](https://doi.org/10.1016/S0140-7007(02)00016-6)
- Beard, N., Straneo, F., & Jenkins, W. (2015). Spreading of Greenland meltwaters in the ocean revealed by noble gases. *Geophysical Research Letters*, 42(18), 7705–7713. <https://doi.org/10.1002/2015GL065003>
- Biddle, L. C., Loose, B., & Heywood, K. J. (2019). Upper ocean distribution of glacial meltwater in the Amundsen Sea, Antarctica. *Journal of Geophysical Research: Oceans*, 124(10), 6854–6870. <https://doi.org/10.1029/2019JC015133>

Acknowledgments

This work was supported by the National Science Foundation Awards ANT-1341630 (B. Loose), ANT-1341717 (S.F.Ackley), ANT-1341606 (S. Stammerjohn), ANT-1543483 (P. Sedwick). The authors are grateful for the thoughtful suggestions of Frank Pavia and three anonymous reviewers, which lead us to include a discussion and quantification of the diffusive gas exchange, among other significant improvements to the manuscript. The authors would like to thank the staff of the Antarctic Support Contractor for their efforts to gather high quality data in the challenging environment of the Ross Sea in late Fall.

- Bigdeli, A., Hara, T., Nguyen, A. T., & Loose, B. (2017). Wave attenuation and gas exchange velocity in marginal sea ice zone. *Journal of Geophysical Research: Oceans*, 123(3), 2293–2304. <https://doi.org/10.1002/2017jc013380>
- Broecker, W., Lynch-Stieglitz, J., Archer, D., Hofmann, M., Maier-Reimer, E., Marchal, O., et al. (1999). How strong is the Harvardton-Bear constraint? *Global Biogeochemical Cycles*, 13(4), 817–820. <https://doi.org/10.1029/1999gb900050>
- Cheon, W. G., Lee, S.-K., Gordon, A. L., Liu, Y., Cho, C.-B., & Park, J. J. (2015). Replicating the 1970s' Weddell Polynya using a coupled ocean-sea ice model with reanalysis surface flux fields. *Geophysical Research Letters*, 42(13), 5411–5418. <https://doi.org/10.1002/2015GL064364>
- Cliff, E., Khatiwala, S., & Schmittner, A. (2021). Glacial deep ocean deoxygenation driven by biologically mediated air–sea disequilibrium. *Nature Geoscience*, 14(1), 43–50. <https://doi.org/10.1038/s41561-020-00667-z>
- Costanza, C. A., Lazzara, M. A., Keller, L. M., & Cassano, J. J. (2016). The surface climatology of the Ross ice shelf Antarctica. *International Journal of Climatology*, 36(15), 4929–4941. <https://doi.org/10.1002/joc.4681>
- Crabeck, O., Galley, R. J., Delille, B., Else, B. G. T., Geilfus, N.-X., Lemes, M., et al. (2015). Imaging air volume fraction in sea ice using non-destructive X-ray tomography. *The Cryosphere Discussions*, 5203–5251. <https://doi.org/10.5194/tcd-9-5203-2015>
- de Lavergne, C., Palter, J. B., Galbraith, E. D., Bernardello, R., & Marinov, I. (2014). Cessation of deep convection in the open Southern Ocean under anthropogenic climate change. *Nature Climate Change*, 4, 278–282. <https://doi.org/10.1038/nclimate2132>
- Dieckmann, G. S., Nehrke, G., Papadimitriou, S., Göttlicher, J., Steninger, R., Kennedy, H., et al. (2008). Calcium carbonate as ikaite crystals in Antarctic sea ice. *Geophysical Research Letters*, 35(8), L08501. <https://doi.org/10.1029/2008gl033540>
- Feltham, D. L., Untersteiner, N., Wettlaufer, J. S., & Worster, M. G. (2006). Sea ice is a mushy layer. *Geophysical Research Letters*, 33(14), L14501. <https://doi.org/10.1029/2006GL026290>
- Frezzotti, M. (1993). Glaciological study in Terra Nova Bay, Antarctica, inferred from remote sensing analysis. *Annals of Glaciology*, 17, 63–71. <https://doi.org/10.3189/S0260305500012623>
- Gade, H. (1979). Melting of ice in sea water: A primitive model with application to the Antarctic ice shelf and icebergs. *Journal of Physical Oceanography*, 9(1), 189–198. [https://doi.org/10.1175/1520-0485\(1979\)009<0189:moiiws>2.0.co;2](https://doi.org/10.1175/1520-0485(1979)009<0189:moiiws>2.0.co;2)
- Garandet, J., Favier, J., & Camel, D. (1994). Segregation phenomena in crystal growth from the melt. *Handbook of Crystal Growth*, 2, 659–705.
- Gordon, A. L., Huber, B., McKee, D., & Visbeck, M. (2010). A seasonal cycle in the export of bottom water from the Weddell Sea. *Nature Geoscience*, 3(8), 551–556. <https://doi.org/10.1038/ngeo916>
- Guest, P. S. (2021). Inside katabatic winds over the Terra Nova Bay polynya: 2. Dynamic and thermodynamic analyses. *Journal of Geophysical Research: Atmospheres*, 126(20), e2021JD034904. <https://doi.org/10.1029/2021JD034904>
- Hamme, R. C., Emerson, S. R., Severinghaus, J. P., Long, M. C., & Yashayaev, I. (2017). Using noble gas measurements to derive air-sea process information and predict physical gas saturations. *Geophysical Research Letters*, 44(19), 9901–9909. <https://doi.org/10.1002/2017GL075123>
- Hamme, R. C., Nicholson, D. P., Jenkins, W. J., & Emerson, S. R. (2019). Using noble gases to assess the ocean's carbon pumps. *Annual Review of Marine Science*, 11(1), 75–103. <https://doi.org/10.1146/annurev-marine-121916-063604>
- Hamme, R. C., & Severinghaus, J. P. (2007). Trace gas disequilibria during deep-water formation. *Deep-Sea Research, Part A: Oceanographic Research Papers*, 54(6), 939–950. <https://doi.org/10.1016/j.dsr.2007.03.008>
- Hood, E. M., Howes, B. L., & Jenkins, W. J. (1998). Dissolved gas dynamics in perennially ice-covered Lake Fryxell, Antarctica. *Deep-Sea Research*, 50(2), 265–272. <https://doi.org/10.4319/lo.1998.43.2.0265>
- Jacobs, S. S., & Giulivi, C. F. (2010). Large multidecadal salinity trends near the Pacific–Antarctic continental margin. *Journal of Climate*, 23(17), 4508–4524. <https://doi.org/10.1175/2010JCLI3284.1>
- Jacobs, S. S., Giulivi, C. F., & Dutrieux, P. (2022). Persistent Ross Sea freshening from imbalance West Antarctic ice shelf melting. *Journal of Geophysical Research: Oceans*, 127(3), e2021JC017808. <https://doi.org/10.1029/2021JC017808>
- Jacobs, S. S., Giulivi, C. F., & Mele, P. A. (2002). Freshening of the Ross Sea during the late 20th century. *Science*, 297(5580), 386–389. <https://doi.org/10.1126/science.1069574>
- Jenkins, A. (1999). The impact of melting ice on ocean waters. *Journal of Physical Oceanography*, 29(9), 2370–2381. <https://doi.org/10.1175/1520-0485>
- Jenkins, W. J. (2020). Using excess ³He to estimate Southern Ocean upwelling time scales. *Geophysical Research Letters*, 47(15), e2020GL087266. <https://doi.org/10.1029/2020GL087266>
- Jenkins, W. J., Lott, D. E., & Cahill, K. L. (2019). A determination of atmospheric helium, neon, argon, krypton, and xenon solubility concentrations in water and seawater. *Marine Chemistry*, 211, 94–107. <https://doi.org/10.1016/j.marchem.2019.03.007>
- Killawee, J. A., Fairchild, I. J., Tison, J.-L., Janssens, L., & Lorrain, R. (1998). Segregation of solutes and gases in experimental freezing of dilute solutions: Implications for natural glacial systems. *Geochimica et Cosmochimica Acta*, 62(23–24), 3637–3655. [https://doi.org/10.1016/S0016-7037\(98\)00268-3](https://doi.org/10.1016/S0016-7037(98)00268-3)
- Liang, J.-H., Deutsch, C., McWilliams, J. C., Baschek, B., Sullivan, P. P., & Chiba, D. (2013). Parameterizing bubble-mediated air-sea gas exchange and its effect on ocean ventilation. *Global Biogeochemical Cycles*, 27(3), 894–905. <https://doi.org/10.1002/gbc.20080>
- Loose, B. (2022). PIPERS noble gases [Dataset]. US Antarctic Program (USAP) Data Center. <https://doi.org/10.15784/601609>
- Loose, B., & Jenkins, W. J. (2014). The five stable noble gases are sensitive unambiguous tracers of glacial meltwater: Loose and Jenkins; noble gases are tracers of meltwater. *Geophysical Research Letters*, 41(8), 2835–2841. <https://doi.org/10.1002/2013GL058804>
- Loose, B., Jenkins, W. J., Moriarty, R., Brown, P., Jullion, L., Naveira Garabato, A. C., et al. (2016). Estimating the recharge properties of the deep ocean using noble gases and helium isotopes. *Journal of Geophysical Research: Oceans*, 121(8), 5959–5979. <https://doi.org/10.1002/2016JC011809>
- Loose, B., Schlosser, P., Smethie, W. M., & Jacobs, S. (2009). An optimized estimate of glacial melt from the Ross Ice Shelf using noble gases, stable isotopes, and CFC transient tracers. *Journal of Geophysical Research*, 114(C8), C08007. <https://doi.org/10.1029/2008JC005048>
- Martin, S., & Kauffman, P. (1981). A field and laboratory study of wave damping by grease ice. *Journal of Glaciology*, 27(96), 283–313. <https://doi.org/10.3189/s0022143000015392>
- Martinerie, P., Raynaud, D., Etheridge, D. M., Barnol, J.-M., & Mazaudier, D. (1992). Physical and climatic parameters which influence the air content in polar ice. *Earth and Planetary Science Letters*, 112(1–4), 1–13. [https://doi.org/10.1016/0012-821x\(92\)90002-d](https://doi.org/10.1016/0012-821x(92)90002-d)
- Matsumura, Y., & Ohshima, K. I. (2015). Lagrangian modelling of frazil ice in the ocean. *Annals of Glaciology*, 56(69), 373–382. <https://doi.org/10.3189/2015aog69a657>
- Morrison, A. K., McC, H. A., England, M. H., & Spence, P. (2020). Warm Circumpolar Deep Water transport toward Antarctica driven by local dense water export in canyons. *Science Advances*, 6, eaav2516. <https://doi.org/10.1126/sciadv.aav2516>
- Nakata, K., Ohshima, K. I., & Nihashi, S. (2021). Mapping of active frazil for Antarctic coastal polynyas, with an estimation of sea-ice production. *Geophysical Research Letters*, 48(6), e2020GL091353. <https://doi.org/10.1029/2020GL091353>
- Namiot, A. Y., & Bukhgalter, E. B. (1965). Clathrates formed by gases in ice. *Journal of Structural Chemistry*, 6, 873–874. <https://doi.org/10.1007/bf00747111>

- Nicholson, D., Emerson, S., Caillon, N., Jouzel, J., & Hamme, R. C. (2010). Constraining ventilation during deepwater formation using deep ocean measurements of the dissolved gas ratios $^{40}\text{Ar}/^{36}\text{Ar}$, N_2/Ar , and Kr/Ar . *Journal of Geophysical Research*, *115*(C11), C11015. <https://doi.org/10.1029/2010jc006152>
- Nicholson, D. P., Emerson, S. R., Khatiwala, S., & Hamme, R. C. (2011). An inverse approach to estimate bubble-mediated air-sea gas flux from inert gas measurements. In *Proceedings on the 6th international symposium on gas transfer at water surfaces* (pp. 223–237). Kyoto University Press Kyoto.
- Nihashi, S., & Ohshima, K. I. (2015). Circumpolar mapping of Antarctic coastal polynyas and landfast sea ice: Relationship and variability. *Journal of Climate*, *28*(9), 3650–3670. <https://doi.org/10.1175/JCLI-D-14-00369.1>
- Ohshima, K. I., Fukamachi, Y., Williams, G. D., Nihashi, S., Roquet, F., Kitade, Y., et al. (2013). Antarctic bottom water production by intense sea-ice formation in the Cape Darnley polynya. *Nature Geoscience*, *6*(3), 235–240. <https://doi.org/10.1038/ngeo1738>
- Ohshima, K. I., Nihashi, S., & Iwamoto, K. (2016). Global view of sea-ice production in polynyas and its linkage to dense/bottom water formation. *Geoscience Letters*, *3*(1), 13. <https://doi.org/10.1186/s40562-016-0045-4>
- Orsi, A. H., & Wiederwohl, C. L. (2009). A recount of Ross Sea waters. *Deep Sea Research Part II: Topical Studies in Oceanography*, *56*(13–14), 778–795. <https://doi.org/10.1016/j.dsr2.2008.10.033>
- Padman, L., Howard, S. L., Orsi, A. H., & Muench, R. D. (2009). Tides of the northwestern Ross Sea and their impact on dense outflows of Antarctic bottom water. *Deep Sea Research Part II: Topical Studies in Oceanography*, *56*(13–14), 818–834. <https://doi.org/10.1016/j.dsr2.2008.10.026>
- Petrelli, P., Bindoff, N., & Bergamasco, A. (2008). The sea ice dynamics of Terra Nova Bay and Ross ice shelf polynyas during a spring and winter simulation. *Journal of Geophysical Research*, *113*(C9), C09003. <https://doi.org/10.1029/2006jc004048>
- Postlethwaite, C. (2002). *Developing a tool for evaluating the role of seasonal sea ice in deep-water formation*. University of Southampton.
- Press, W. H., Teukolsky, S. A., Vetterling, W., & Flannery, B. (2007). *Numerical recipes: The art of scientific computing* (3rd ed.). Cambridge University Press.
- Schick, K. E. (2018). *Influences of weather and surface variability on sensible heat fluxes in Terra Nova Bay, Antarctica*. University of Colorado.
- Seltzer, A. M., Pavia, F. J., Ng, J., & Severinghaus, J. P. (2019). Heavy noble gas isotopes as new constraints on the ventilation of the deep ocean. *Geophysical Research Letters*, *46*(15), 8926–8932. <https://doi.org/10.1029/2019GL084089>
- Sigman, D. M., Hain, M. P., & Haug, G. H. (2010). The polar ocean and glacial cycles in atmospheric CO_2 concentration. *Nature*, *466*(7302), 47–55. <https://doi.org/10.1038/nature09149>
- Silvano, A., Foppert, A., Rintoul, S. R., Holland, P. R., Tamura, T., Kimura, N., et al. (2020). Recent recovery of Antarctic bottom water formation in the Ross Sea driven by climate anomalies. *Nature Geoscience*, *13*(12), 780–786. <https://doi.org/10.1038/s41561-020-00655-3>
- Silvano, A., Rintoul, S., Peña-Molino, B., Hobbs, W. R., van Esmee, W., Aoki, S., et al. (2018). Freshening by glacial meltwater enhances melting of ice shelves and reduces formation of Antarctic bottom water. *Science Advances*, *4*, eaap9467. <https://doi.org/10.1126/sciadv.aap9467>
- Smethie, W. M., & Jacobs, S. S. (2005). Circulation and melting under the Ross ice shelf: Estimates from evolving CFC, salinity and temperature fields in the Ross Sea. *Deep-Sea Research*, *52*(6), 959–978. <https://doi.org/10.1016/j.dsr.2004.11.016>
- Stanley, R. H. R., Baschek, G., Lott, D. E. I., & Jenkins, W. J. (2009). A method for measuring noble gases and their isotopic ratios using programmed multistage cryogenic trapping and a combination of quadrupole and magnetic sector mass spectrometers. *Geochemistry, Geophysics, Geosystems*, *10*(5), Q05008. <https://doi.org/10.1029/2009GC002429>
- Stanley, R. H. R., Jenkins, W. J., Lott, D. E. I., & Doney, S. C. (2009). Noble gas constraints on air-sea gas exchange and bubble fluxes. *Journal of Geophysical Research*, *114*(C11), C11020. <https://doi.org/10.1029/2009JC005396>
- Stephens, B. B., & Keeling, R. F. (2000). The influence of Antarctic sea ice on glacial-interglacial CO_2 variations. *Nature*, *404*(6774), 171–174. <https://doi.org/10.1038/35004556>
- Stute, M., & Schlosser, P. (1993). Principles and applications of the noble gas paleothermometer. In *Climate change in continental isotopic records* (pp. 89–100). American Geophysical Union.
- Takahashi, T., Sutherland, S. C., Wanninkhof, R., Sweeney, C., Feely, R. A., Chipman, D. W., et al. (2009). Climatological mean and decadal change in surface ocean pCO_2 , and net sea-air CO_2 flux over the global oceans. *Deep-Sea Research Part II*, *56*(8–10), 554–577. <https://doi.org/10.1016/j.dsr2.2008.12.009>
- Tamura, T., Ohshima, K., & Nihashi, S. (2008). Mapping of sea ice production for Antarctic coastal polynyas. *Geophysical Research Letters*, *35*(7), L07606. <https://doi.org/10.1029/2007GL032903>
- Thomas, D. N., & Dieckmann, G. S. (2010). *Sea ice* (2nd ed.). Wiley-Blackwell.
- Thompson, L., Smith, M., Thomson, J., Stammerjohn, S., Ackley, S., & Loose, B. (2020). Frazil ice growth and production during katabatic wind events in the Ross Sea, Antarctica. *The Cryosphere*, *14*(10), 3329–3347. <https://doi.org/10.5194/tc-14-3329-2020>
- Tison, J.-L., Maksym, T., Fraser, A. D., Corkill, M., Kimura, N., Nosaka, Y., et al. (2020). Physical and biological properties of early winter Antarctic sea ice in the Ross Sea. *Annals of Glaciology*, *61*(83), 241–259. <https://doi.org/10.1017/aog.2020.43>
- Toggweiler, J. R., Gnanadesikan, A., Carson, S., Murnane, R., & Sarmiento, J. L. (2003). Representation of the carbon cycle in box models and GCMs: 1. Solubility pump. *Global Biogeochemical Cycles*, *17*. <https://doi.org/10.1029/2001GB001401>
- Top, Z., Martin, S., & Becker, P. (1988). A laboratory study of dissolved noble gas anomaly due to ice formation. *Geophysical Research Letters*, *15*(8), 796–799. <https://doi.org/10.1029/GL015i008p00796>
- Wettlaufer, J. S. (1992). Directional solidification of salt water: Deep and shallow cells. *Europhysics Letters*, *19*(4), 337–342. <https://doi.org/10.1209/0295-5075/19/4/015>
- Williams, G., Herraiz-Borreguero, L., Roquet, F., Tamura, T., Ohshima, K. I., Fukamachi, Y., et al. (2016). The suppression of Antarctic bottom water formation by melting ice shelves in Prydz Bay. *Nature Communications*, *7*, 1–9. <https://doi.org/10.1038/ncomms12577>

References From the Supporting Information

- Malone, J. L., Castro, M. C., Hall, C. M., Doran, P. T., Kenig, F., & McKay, C. P. (2010). New insights into the origin and evolution of Lake Vida, McMurdo Dry Valleys, Antarctica—A noble gas study in ice and brines. *Earth and Planetary Science Letters*, *289*(1–2), 112–122. <https://doi.org/10.1016/j.epsl.2009.10.034>